

## Comparison of direct numerical simulation databases of turbulent channel flow at $Re_\tau = 180$

A. W. Vreman<sup>1,a)</sup> and J. G. M. Kuerten<sup>2</sup>

<sup>1</sup>*AkzoNobel, Research Development and Innovation, Process Technology, P.O. Box 10, 7400 AA Deventer, The Netherlands*

<sup>2</sup>*Department of Mechanical Engineering, Eindhoven University of Technology, P.O. Box 513, 5600 MB Eindhoven, The Netherlands and Faculty EEMCS, University of Twente, P.O. Box 217, 7500 AE Enschede, The Netherlands*

(Received 23 August 2013; accepted 16 December 2013; published online 8 January 2014)

Direct numerical simulation (DNS) databases are compared to assess the accuracy and reproducibility of standard and non-standard turbulence statistics of incompressible plane channel flow at  $Re_\tau = 180$ . Two fundamentally different DNS codes are shown to produce maximum relative deviations below 0.2% for the mean flow, below 1% for the root-mean-square velocity and pressure fluctuations, and below 2% for the three components of the turbulent dissipation. Relatively fine grids and long statistical averaging times are required. An analysis of dissipation spectra demonstrates that the enhanced resolution is necessary for an accurate representation of the smallest physical scales in the turbulent dissipation. The results are related to the physics of turbulent channel flow in several ways. First, the reproducibility supports the hitherto unproven theoretical hypothesis that the statistically stationary state of turbulent channel flow is unique. Second, the peaks of dissipation spectra provide information on length scales of the small-scale turbulence. Third, the computed means and fluctuations of the convective, pressure, and viscous terms in the momentum equation show the importance of the different forces in the momentum equation relative to each other. The Galilean transformation that leads to minimum peak fluctuation of the convective term is determined. Fourth, an analysis of higher-order statistics is performed. The skewness of the longitudinal derivative of the streamwise velocity is stronger than expected ( $-1.5$  at  $y^+ = 30$ ). This skewness and also the strong near-wall intermittency of the normal velocity are related to coherent structures. © 2014 AIP Publishing LLC. [<http://dx.doi.org/10.1063/1.4861064>]

### I. INTRODUCTION

In 1987, Kim, Moin, and Moser<sup>1</sup> performed the first Direct Numerical Simulation (DNS) of fully developed incompressible turbulent channel flow. The Reynolds number based on friction velocity and channel half width was 180. The simulation was repeated in 1999 by Moser, Kim, and Mansour<sup>2</sup> with the same numerical method and a slightly different computational domain. In that paper, referred to as MKM hereafter, the results were compared with DNS of turbulent channel flows at higher Reynolds numbers. The databases of the simulations presented in MKM were published on the world-wide web in 2001. These two pioneering papers belong to the most influential papers in the field of DNS of turbulent flows. Since 1987 many papers on DNS of turbulent channel flow have appeared in the literature, see, for example, Refs. 3–9, see also the review by Kim.<sup>10</sup> The transition process from laminar to fully developed channel flow has also been simulated by means of DNS, see, for example, Refs. 11 and 12.

As far as we know, there exists no systematic comparison of different DNS databases of fully developed turbulent channel flow at the same Reynolds number. A Reynolds number appearing

---

<sup>a)</sup>E-mail: [bert.vreman@akzonobel.com](mailto:bert.vreman@akzonobel.com)

TABLE I. Overview of publicly accessible DNS databases and four databases presented in this paper. The domain lengths are normalized with channel half-width  $H$ . The maximum grid sizes are listed in wall units. The averaging time  $T$  is normalized with  $Hu_\tau$ . FC represents a Fourier-Chebyshev method and FD a staggered finite difference method (fourth-order in streamwise and spanwise, second-order in normal direction).

Database	$Re_\tau$	Domain		Grid (max)			$T$	Method	Centerline values			
		$L_x$	$L_z$	$h_x^+$	$h_y^+$	$h_z^+$			$U$	$u_{rms}$	$v_{rms}$	$w_{rms}$
Moser, Kim, and Mansour <sup>2</sup>	178.1	$4\pi$	$\frac{4}{3}\pi$	17.7	4.4	5.9	?	FC	18.30	0.8140	0.6118	0.5893
Abe, Kawamura, and Matsuo <sup>4</sup>	180.0	12.8	6.4	9.0	5.9	4.5	40	FD	18.64	0.8054	0.6368	0.6041
Del Álamo and Jiménez <sup>5</sup>	185.6	$12\pi$	$4\pi$	13.7	6.1	6.9	50	FC	18.28	0.7892	0.6062	0.6068
Kozuka, Seki, and Kawamura <sup>9</sup>	180.0	6.5	3.2	0.56	0.97	1.1	3.1	FD	18.55	0.8084	0.6410	0.6280
FD1 (this paper)	180.0	$4\pi$	$\frac{4}{3}\pi$	8.8	4.4	5.9	1300	FD	18.42	0.7976	0.6154	0.6103
FD2 (this paper)	180.0	$4\pi$	$\frac{4}{3}\pi$	4.4	2.2	2.9	200	FD	18.28	0.7949	0.6162	0.6139
S1 (this paper)	180.0	$4\pi$	$\frac{4}{3}\pi$	17.7	4.4	5.9	161	FC	18.25	0.7974	0.6149	0.6151
S2 (this paper)	180.0	$4\pi$	$\frac{4}{3}\pi$	5.9	2.9	3.9	200	FC	18.28	0.7971	0.6166	0.6140

frequently in the literature of DNS of turbulent channel flow is  $Re_\tau \approx 180$ . An overview of simulations for domain sizes and resolutions of this Reynolds number is shown in Table I. The first four simulations have been performed by others and the statistical databases are publicly accessible on internet. The last four simulations are the simulations presented in this paper, and corresponding databases are available at [www.vremanresearch.nl](http://www.vremanresearch.nl).

The centerline values of four standard statistical profiles have been included in Table I. There appears to be a large variation among the results reported in the literature. For example, the variation of the reported centerline values of the root-mean-square of the spanwise velocity fluctuation among different cases is approximately 10%. It is not evident at all that the variation is caused by the different domain sizes used in the simulations. A first question that arises is whether for a given domain size a unique statistical solution exists. Although this uniqueness is usually assumed, it is not a theoretically proven consequence of the Navier-Stokes equations. A second question that arises is whether in the known databases the resolution was sufficiently fine and the averaging time was sufficiently large to expect a relative accuracy of basic statistical profiles of say less than 1%. Since DNS is a simulation technique that solves by definition all physical scales, the aim to predict basic quantities within 1% is reasonable.

To address these research questions, we have performed DNS of turbulent channel flow at  $Re_\tau = 180$  in the same domain as MKM (the most cited DNS database of this flow). Two different codes were used, indicated by FD (finite difference) and S (spectral). The finite difference code is staggered and pressure-based (projection method). The spectral code is an independent implementation of the non-pressure-based Fourier-Chebyshev method used in MKM. For each code long-time simulations were performed on two grids, a grid compliant with standard resolution requirements and a refined grid.

There are a number of reasons why statistical results obtained from two simulations performed at the same Reynolds number could differ: (1) the streamwise and spanwise lengths of the computational domain, (2) statistical errors, (3) discretization errors, (4) programming errors, (5) non-uniqueness of a statistically stationary state, and (6) forcing method. To reduce the effect of the streamwise and spanwise lengths of the computational domain, simulations in computational domains larger than those in Refs. 1 and 2 have been reported by Del Álamo and Jiménez<sup>5</sup> and others.<sup>6,8</sup> It is not yet clear how large the domain should be to have no influence on turbulence statistics anymore (if possible at all). The subject of the present paper is not the issue how large the computational domain should be, but the analysis of the other five possible causes (2–6). Due to the required computational effort, this analysis can be performed best if the domain size and also the Reynolds number are not too large. Therefore,  $Re_\tau = 180$  and the domain used by MKM were chosen. A comparison of results obtained with different codes is useful in a study of reproducibility. Besides, a systematic comparison between results obtained with different codes provides a quantification of the maximum effect of possible programming errors.

In the present paper we will present detailed results of the last four databases in Table I and compare the results with those of MKM where possible. In Sec. II, we will describe the numerical

methods and the simulation cases in more detail. In Sec. III, we will compare the common type of profiles, profiles of mean flow, the Reynolds stresses, the pressure variance, and the diagonal components of the dissipation. In Sec. IV, we will compare velocity and pressure gradient spectra (velocity and pressure spectra multiplied with the square of the wavenumber). In Sec. V, we will present the statistical profiles of the distinct terms in the momentum equations. In Sec. VI, we will consider higher-order statistical data, such as velocity derivative skewness, and skewness and flatness of primary fluctuations. Finally, we will formulate the conclusions in Sec. VII.

## II. DEFINITION OF SIMULATIONS

The direct numerical simulations are simulations of incompressible plane channel flow at  $Re_\tau = 180$  in the domain  $4\pi H \times 2H \times \frac{4}{3}H$ . The streamwise, normal, and spanwise directions are denoted by  $x$ ,  $y$ , and  $z$ , respectively. The streamwise, normal, and spanwise velocity components are denoted by  $u$ ,  $v$ , and  $w$ , respectively. In the simulations  $H = 1$ . Periodic boundary conditions are used in the streamwise and spanwise directions, while no-slip boundary conditions are applied at the two walls. Unless mentioned otherwise, the simulations use forcing by constant pressure gradient, represented by the forcing term  $(1, 0, 0)$  in the vector momentum equation. As a consequence,  $u_\tau = (v d\bar{u}/dy)_{wall}^{1/2} = 1$  if the size of the time averaging interval  $T$  approaches infinity. The viscosity  $\nu$  equals  $1/180$ , such that the Reynolds number  $Re_\tau = u_\tau H/\nu$  equals  $180$  and  $y^+ = 180y$ , with respect to the left-wall, which is located at  $y = 0$ .

First, the finite difference method is described. It was used for simulations FD1 and FD2, specified in Table I. The finite difference code is based on a staggered grid.<sup>13</sup> The grid in the homogeneous directions ( $x$  and  $z$ ) is uniform. The grid in the normal direction is nonuniform and smoothly stretched with the use of the tangent hyperbolic function. The time-discretization is a fully explicit second-order three-stage Runge-Kutta method with stage coefficients  $1/3$ ,  $1/2$ , and  $1$ , in fact the three-stage variant of the four-stage method proposed in Ref. 16. The pressure-based projection method is embedded within each stage, which means that an intermediate update of the velocity is obtained using the convective and viscous terms only, then a Poisson equation for the pressure is solved (with a direct method in this case), and then the new stage velocity is obtained by subtracting the pressure gradient contribution from the intermediate velocity. The finite difference simulations use a simple initial condition, a function of  $y$  plus a divergence-free large-amplitude two-modal sinusoidal perturbation. Turbulence develops after several time units, the statistical averaging is started at time  $t = 10H/u_\tau$ .

The spatial discretization is fourth-order in the homogeneous directions only, the discretization in the normal direction is the standard second-order accurate method, like in Ref. 14. The convective terms are discretized in the momentum-conserving divergence form. The divergence form of the convective terms requires velocities to be interpolated from one staggered location to the cell-face of the same or another velocity component. All interpolations in the  $y$ -direction are second-order accurate (weights  $\frac{1}{2}$  and  $\frac{1}{2}$ ), but all interpolations in the  $x$ - and  $z$ -direction are fourth-order accurate. For example, the discretization of  $\partial(uu)/\partial x$  at grid point  $i$  ( $i$  is the index of the  $x$ -direction) is defined by

$$\frac{9}{8h_x}(a_{i+\frac{1}{2}} - a_{i-\frac{1}{2}}) - \frac{1}{24h_x}(a_{i+\frac{3}{2}} - a_{i-\frac{3}{2}}), \quad (1)$$

where  $a$  denotes the flux  $uu$  in the  $u$ -equation. The velocity  $u$  in  $a = uu$  is given by the fourth-order interpolation

$$u_{i-\frac{1}{2}} = \frac{9}{16}(u_i + u_{i-1}) - \frac{1}{16}(u_{i+1} - u_{i-2}). \quad (2)$$

This convective scheme is different from the skew-symmetric fourth-order staggered methods used in Refs. 4, 14, and 15. It is also different from the rotational form, which has been reported to be relatively inaccurate in combination with a second-order finite difference method in the wall normal direction.<sup>17</sup> The present relatively straightforward convective scheme was chosen, because it was found to produce approximately two times lower truncation error than the corresponding

skew-symmetric scheme on the same grid. Unlike the skew-symmetric and rotational forms, the present convective scheme allows some truncation error in the energy conservation property. It is nonetheless a robust method in cases where the effect of the convective truncation error is small compared to the physical dissipation. DNS is such a case. As a validation the energy produced by the convective scheme (integral of innerproduct of convective term and  $\mathbf{u}$ ) was computed and compared with the dissipation by the viscous term (integral of innerproduct of viscous term and  $\mathbf{u}$ ). It appeared to be very small at all times, about 0.2% of the dissipation by the viscous term in case FD1 and about 0.05% in case FD2. With respect to the viscous terms, the  $y$ -derivatives are discretized with the standard three-point stencil, while the  $x$ - and  $z$ -derivatives in the velocity Laplacians are discretized with the compact fourth-order stencil (five points), which is a Richardson extrapolation of the second-order three-point stencil.<sup>15</sup> To compute the viscous terms near the wall fourth-order extrapolation of the tangential velocities across the boundary is used. For the normal velocity and pressure no extrapolation is required.

The number of cells in cases FD1 and FD2 equals  $256 \times 128 \times 128$  and  $512 \times 256 \times 256$ , respectively. The time step in FD1 and FD2 is 0.001 and 0.0005, respectively. The minimum grid size, the size in the normal direction of the first pressure cell adjacent to the wall, is  $h_y^+ = 0.98$  for FD1 and  $h_y^+ = 0.49$  for FD2. To investigate the influence of statistical averaging, a variant of FD1 is included, FD1a, which is the same as FD1, except for the statistical averaging. Like FD2, FD1a is averaged over a time interval with length  $T = 200H/u_\tau$ , while  $T = 1300H/u_\tau$  is used in case FD1 (see Table I).

In simulations S1 and S2, also listed in Table I, the spectral method used in MKM<sup>2</sup> and described in Ref. 1 is applied. The present implementation of that method is the code also used in Refs. 18, 19. The spectral method is based on the equations of the normal vorticity component and the Laplacian of the normal velocity; as such this method is not pressure-based. The pressure is obtained by solving a Poisson equation in a post-processing step. The method is a spectral tau method with Fourier modes in the homogeneous directions and Chebyshev modes in the normal direction. The code uses dealiasing in the homogeneous directions, by means of the 3/2-rule. The time integration is second-order accurate and performed with the hybrid explicit/implicit three-stage Runge-Kutta method specified in Ref. 20. The number of grid points used in case S1 is the same as in MKM ( $128 \times 129 \times 128$ ), while it is  $384 \times 193 \times 192$  in case S2. The time step in S1 and S2 is 0.0005 and 0.00025, respectively, a factor two smaller than in the FD cases. A spectral method usually requires a smaller time step for numerical stability than finite difference methods. Consider, for example, the convective derivative  $c\partial(\exp(ikx))/\partial x$ , where  $c$  is a constant. The numerical representation is given by  $ick'\exp(ikx)$  where  $k'$  is the modified wavenumber which is a function of wavenumber  $k$ . The modified wavenumber depends on the spatial discretization; for the spectral method  $k' = k$ . A condition  $CFL \leq 1$  for all wavenumbers implies  $\Delta t \leq 1/(c\max(k'))$ . For the present fourth-order finite difference method  $\max(k') = 0.45\pi/h_x$ , while for the spectral method  $\max(k') = \pi/h_x$ ; thus, the spectral method requires a smaller  $\Delta t$ .

Simulations S1, S2 and the finite difference simulations are performed with a constant (pressure gradient) forcing, while in MKM a time-dependent forcing was applied to keep the volume flow constant. To address the effect of the different forcing, a variant of S1 is included, S1a, which is the same as S1, except that in S1a the volume flow is constant and the forcing time-dependent, like in MKM. In the spectral case the forcing term appears in the equation for mode (0, 0, 0). Unlike the other modes, this mode is not solved from the vorticity and velocity Laplacian equation but from the momentum equations.

### III. TURBULENCE STATISTICS OF STANDARD QUANTITIES

In this section the turbulence statistics of a range of common quantities extracted from the simulations FD1, FD2, S1, and S2 will be shown and compared with MKM. The quantitative differences between the different databases will also be shown. Profiles of the additional two simulations, FD1a and S1a, defined in Sec. II, will not be included into the figures, but the results will be discussed.

The statistical mean (or Reynolds average) at position  $y_1$  is implemented as the combined average over time and the two  $x$ - $z$  planes at  $y = y_1$  and  $2H - y_1$ , taking into account the appropriate centerline symmetry condition for the profile under consideration. Each variable can be split into a mean (averaged) and fluctuating part, for example,  $u = \bar{u} + u'$ , where  $\bar{u}$  (also  $U$ ) is the mean and  $u'$  is the fluctuating part. The standard deviation, or root-mean-square (rms) value of the fluctuating part, is defined by  $u_{rms} = \overline{u'u'}^{1/2}$ , which is for brevity also referred to as the fluctuation of  $u$ . Similarly, the fluctuations of  $v$ ,  $w$ , and  $p$  are defined by  $v_{rms} = \overline{v'v'}^{1/2}$ ,  $w_{rms} = \overline{w'w'}^{1/2}$ , and  $p_{rms} = \overline{p'p'}^{1/2}$ , respectively. The dissipation in the transport equation of  $\overline{u'u'}$  is defined by  $\epsilon_u = 2\nu|\nabla u'|^2$ , and similarly  $\epsilon_v$  and  $\epsilon_w$  are defined. The turbulent dissipation in the kinetic energy equation is defined by  $\epsilon = (\epsilon_u + \epsilon_v + \epsilon_w)/2$ .

Most statistics involve the evaluation of products. In the spectral cases S1 and S2, these products are computed in physical space, after extending the wavenumber range with the 3/2-rule in the homogeneous directions. In fact each quantity used in physical space is obtained by the inverse Fourier transform using the 3/2-rule in homogeneous directions. The number of grid nodes in physical space is therefore also multiplied with 3/2 in the homogeneous directions. In the spectral cases, the products and the planar average of any required quantity are computed on this grid. In the finite difference cases, the original normal location (central or staggered) is maintained in the statistics where possible.

In the finite difference cases, the pressure is defined at cell centers and the velocity components at cell faces. This makes the evaluation of the turbulent dissipation nontrivial. It is important to compute the dissipation without throwing away small-scale information by unnecessary interpolations. Consistent with the discretization of the velocity Laplacians in the Navier-Stokes code, the first-order velocity derivative  $\partial u_j/\partial x_k$  in the dissipation has been obtained on the appropriate location half-way two (staggered) points in the  $x_k$ -direction where the velocity  $u_j$  is defined. For example,  $\partial u/\partial x$  in the post-processing is computed at location  $i + \frac{1}{2}$ , using the four values  $u_{i-1}$ ,  $u_i$ ,  $u_{i+1}$ , and  $u_{i+2}$ . This procedure implies that the nine post-processed velocity derivatives are defined at different locations. To find the dissipation at cell centers, the nine profiles of the variances of the velocity derivatives are determined first, without any interpolation. Some of these profiles are defined at  $y_c$  (the  $y$ -values of the cell centers) and others are defined at  $y_s$  (the  $y$ -values of the cell faces pointing in the normal direction). Subsequently, the latter profiles are interpolated to  $y_c$ -locations by averaging over the two adjacent  $y_s$ -points.

For the cases with constant pressure gradient forcing the numerical value of  $u_\tau$  is very close to 1: 1.00000 for FD1 ( $T = 1300$ ), 1.00007 for FD1a ( $T = 200$ ), 0.99996 for FD2 ( $T = 200$ ), 1.00043 for S1 ( $T = 161$ ), and 0.99990 for S2 ( $T = 200$ ). The statistics of these five simulations have not been normalized with the computational  $u_\tau$ . In the case with constant volume flow (S1a) the computational value of  $u_\tau$  is 0.995616 ( $T = 200$ ), such that  $Re_\tau = 179.2$ . The statistics of S1a have been normalized with the computational  $u_\tau$  before comparison with S1.

The left-hand sides of Figs. 1–4 show the profiles of the mean streamwise velocity (Fig. 1), the fluctuations of  $u$ ,  $v$ ,  $w$  (Fig. 2), the fluctuation of  $p$  (Fig. 3), and the dissipations  $\epsilon_u$ ,  $\epsilon_v$ , and  $\epsilon_w$  (Fig. 4). On the scale of these figures, we observe several small but noticeable differences between S1, S2, FD1, FD2, and MKM. In the figures of the normal and spanwise intensities, we observe relatively large differences between S1, S2, FD1, and S2 on the one hand and MKM on the other hand.

To investigate the differences between the five cases in more detail we express the differences between the curves as relative deviations. The right-hand sides of Figs. 1–4 show the relative deviations between case A and simulation S2, for any of the five cases A shown in the left-hand side of the figure. The relative deviation of a quantity  $Q$  of case A with respect to case S2 is defined by

$$\delta Q[A;S2](y) = (Q_A(y) - Q_{S2}(y))/Q_{S2}(y). \quad (3)$$

The trivial deviation  $\delta Q[S2; S2](y)$  equals zero. The deviations were computed after interpolation of the profiles to a uniform grid,  $y^+(j) = j$  for integers  $1 \leq j \leq 180$ . A cubic spline interpolation routine was used. However, the curves on the left-hand sides of the figures are the original (non-interpolated) profiles.

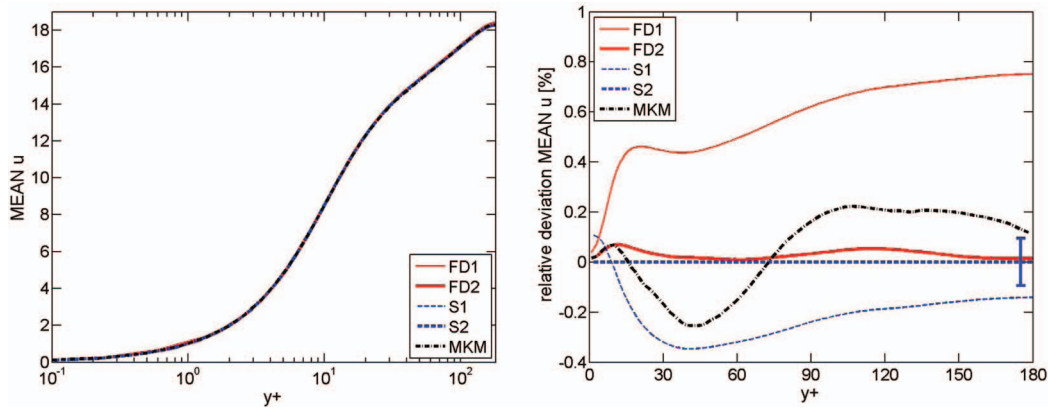


FIG. 1. Mean streamwise velocity for FD1 (thin solid), FD2 (thick solid), S1 (thin dashed), S2 (thick dashed), and MKM (thick dashed-dotted). Left:  $U$ . Right: the corresponding relative deviations  $\delta U[\text{FD1}; \text{S2}]$ ,  $\delta U[\text{FD2}; \text{S2}]$ ,  $\delta U[\text{S1}; \text{S2}]$ ,  $\delta U[\text{S2}; \text{S2}]$ , and  $\delta U[\text{MKM}; \text{S2}]$  (%).

To estimate the statistical uncertainty of profiles obtained by averaging over an interval of about 200 time units, case FD1, which is the case that requires the smallest computational effort per time step, was simulated for a very long time (more than 1300 time units). From the same run statistics were computed for  $T = 200$ ; these results are referred to as F1a. Since FD1 ( $T = 1300$ ) has most probably a much lower statistical error than FD1a ( $T = 200$ ), the maximum statistical relative error of a quantity  $Q$  in case FD1a can be estimated by the maximum of the absolute value of the relative difference between the two profiles:

$$s_Q = \max|\delta Q[\text{FD1a}; \text{FD1}](y)|. \quad (4)$$

Although simulation FD1 is not the most accurate of the simulations presented in this paper, simulation FD1 is still quite accurate. The maximum statistical error of simulation FD1a ( $s_Q$ ) is therefore expected to be a suitable estimate of the statistical error of the profiles of FD2 and S2, which, like those of FD1a, were obtained for  $T = 200$ . For each quantity  $Q$  in this section, the statistical uncertainty  $s_Q$  is shown as an error bar  $\pm s_Q$  in the corresponding figure with the relative deviations. The numerical values of  $s_Q$  are shown in the first line of Table II. The statistical error of FD1 ( $T = 1300$ ) is most probably much smaller than  $s_Q$ , while the statistical uncertainty of case S1 is expected to be slightly larger than  $s_Q$  (in case S1 the averaging interval is somewhat shorter than 200 time units). Although the statistical averaging time was not reported in MKM, the present comparison indicates that the statistical uncertainty of the MKM case is probably larger than  $s_Q$ .

An alternative approach to compute a statistical uncertainty is to partition the time interval of 200 time units into  $n$  equally sized parts and to compute the average for each part.<sup>5</sup> An unbiased estimate of the statistical error of the total average is then given by the standard deviation of the partial results divided by the square root of  $n - 1$ . However, that estimate is only valid if the partial averages are uncorrelated, which is not necessarily the case,<sup>5</sup> since the turbulence is temporally correlated.

Figure 1 shows that for each case the relative deviation with respect to S2 is smaller than 1%. If the deviation for cases FD1, FD2, and S1 is larger than  $2s_Q$ , the deviation is probably not only a statistical effect. The deviation between FD2 and S2 is smaller than  $2s_Q$  everywhere, *i.e.*, the deviation between the two fine grid runs is within the statistical tolerance, which is about 0.2% in case of the mean flow.

The relative deviations of the velocity and pressure fluctuations (Figs. 2 and 3) are much larger than those of the mean flow. The deviations for the standard resolution cases (FD1, S1, MKM) are clearly larger than 1% at several locations, at some locations much larger. Since the statistical difference between FD1 and S2, or between S1 and S2, is not expected to be larger than  $2s_Q$ , which is less than 0.8% for the four fluctuations, the deviations of FD1 and S1 cannot be attributed to the statistical error only. However, the maximum deviations between FD2 and S2 are much smaller,

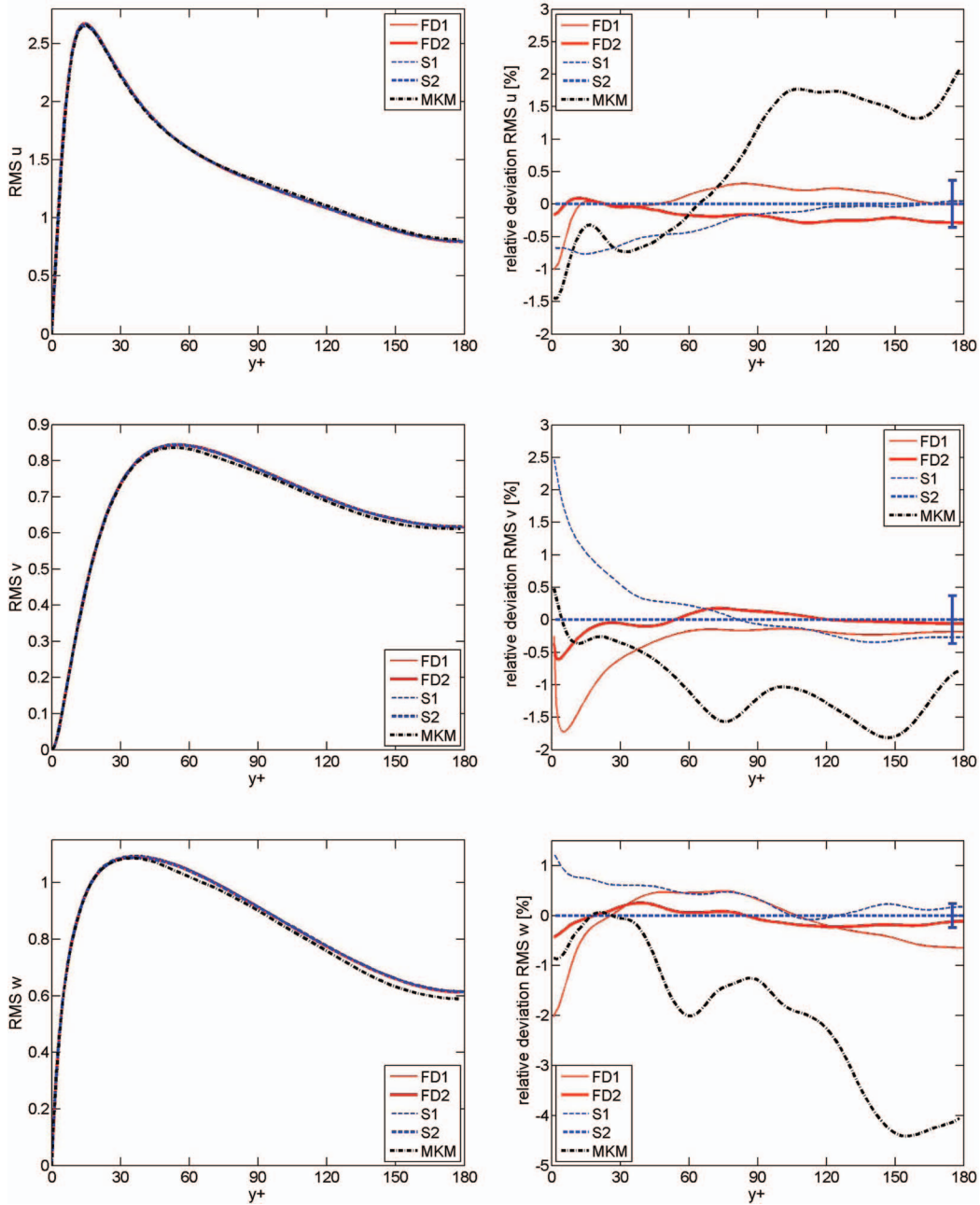


FIG. 2. Velocity fluctuations for FD1 (thin solid), FD2 (thick solid), S1 (thin dashed), S2 (thick dashed), and MKM (thick dashed-dotted). Left:  $u_{rms}$  (top),  $v_{rms}$  (middle), and  $w_{rms}$  (bottom). Right: the corresponding relative deviations  $\delta Q[\text{FD1}; \text{S2}]$ ,  $\delta Q[\text{FD2}; \text{S2}]$ ,  $\delta Q[\text{S1}; \text{S2}]$ ,  $\delta Q[\text{S2}; \text{S2}]$ , and  $\delta Q[\text{MKM}; \text{S2}]$  (%), where  $Q$  is  $u_{rms}$  (top),  $v_{rms}$  (middle), or  $w_{rms}$  (bottom).

0.4%, 0.6%, 0.4%, and 0.5% for the primary fluctuations ( $u_{rms}$ ,  $v_{rms}$ ,  $w_{rms}$ , and  $p_{rms}$ , respectively). The deviations for the dissipation profiles (Fig. 4) are generally larger than those for the primary fluctuations. However, also for the dissipations, the deviation between FD2 and S2 is the smallest one of the nontrivial deviations: 0.8%, 1.8%, and 1.5% for  $\epsilon_u$ ,  $\epsilon_v$ , and  $\epsilon_w$ , respectively.

Table II contains the absolute maxima of the relative deviations shown in Figs. 1–4. It is clear that cases FD2 and S2 are more accurate than the other cases. It seems safe to conclude that the maximum relative error in cases FD2 and S2 is below 0.2% for the mean flow, below 1% for the fluctuations,  $u_{rms}$ ,  $v_{rms}$ ,  $w_{rms}$ , and  $p_{rms}$ , and below 2% for  $\epsilon_u$ ,  $\epsilon_v$ , and  $\epsilon_w$ . The results in Secs. IV–VI

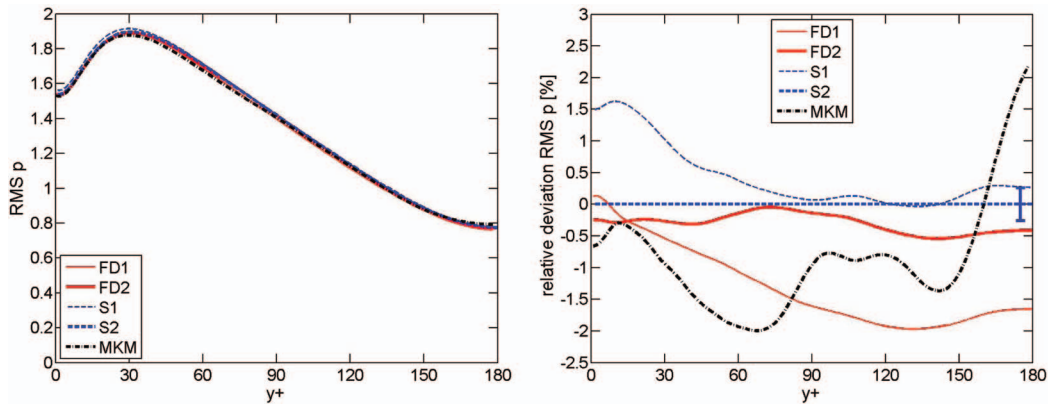


FIG. 3. Pressure fluctuation for FD1 (thin solid), FD2 (thick solid), S1 (thin dashed), S2 (thick dashed), and MKM (thick dashed-dotted). Left:  $p_{rms}$ . Right: the corresponding relative deviations  $\delta p_{rms}[FD1; S2]$ ,  $\delta p_{rms}[FD2; S2]$ ,  $\delta p_{rms}[S1; S2]$ ,  $\delta p_{rms}[S2; S2]$ , and  $\delta p_{rms}[MKM; S2]$  (%).

will confirm that the difference between FD2 and S2 is much smaller than the difference between FD1 and S1, between FD1 and FD2, and between S1 and S2. This reproducibility supports the hypothesis that the Navier-Stokes solutions for turbulent channel flow in a given domain share the same unique statistically stationary state.

We will finish this section with a discussion of the results obtained with fixed volume flow (S1a) instead of the constant forcing term in the other cases, since in the MKM simulation the volume flow was also held fixed. In Table II the maximum relative deviations between S1a and S1 and between S1a and S2 are shown (lines 7 and 8); constant forcing is used in cases S1 and S2. The numbers appear to be comparable or somewhat smaller than the maximum relative deviation between S1 and S2 (line 4). In particular, the differences between S1a and S1 (line 7) are generally smaller than the differences between MKM and S1 (line 4). Thus, the forcing method is most probably not the main reason for the differences observed between MKM and the present runs in Figs. 1–4.

#### IV. SPECTRA

Streamwise spectra premultiplied with streamwise wavenumber  $k_x^2$  are shown in Fig. 5, for  $u$ ,  $v$ ,  $w$ , and  $p$ . Spanwise spectra premultiplied with spanwise wavenumber  $k_z^2$  are shown in Fig. 6. All spectra shown apply to  $y^+ = 30$ , which was found to be a representative value, for the phenomena observed. In Fig. 5, the symbols  $E_{uu}$ ,  $E_{vv}$ ,  $E_{ww}$ , and  $E_{pp}$  represent the standard streamwise velocity and pressure spectra. The integral of  $k_x^2 E_{uu}$  over  $k_x$  is proportional to the cross-sectional average of  $(\partial u' / \partial x)^2 = \overline{(\partial u / \partial x)^2}$ . Analogous relations hold for the other variables. For this reason the premultiplied velocity spectra are also called dissipation spectra. The premultiplied pressure spectrum in Fig. 5 gives information of the relevance of small scales in  $-\partial p / \partial x$ , one of the terms in the momentum equation.

The tails of the spectra of the spectral simulations S1 and MKM display (numerically induced) cusps (Fig. 5). The tail values have not dropped much, relative to the peak values. Consider, for example,  $k_x^2 E_{vv}$ , where the tail values of S1 and MKM are more than 10% of the peak values, so the drop is less than an order of magnitude. For sufficiently high  $k$  ( $k \rightarrow \infty$ , infinite resolution) not only the velocity spectra but also the dissipation spectra are expected to converge (exponentially) to zero. If a spectrum is still large for the highest resolved  $k_x$ , this is an indication that the corresponding quantity is not fully resolved.

To clarify this further Fig. 7 shows the first two spectra of Fig. 5 without the logarithmic scaling of the axes. It is clear that not all wavenumbers contributing to these quantities are resolved in cases FD1 and S1. Since the high wavenumber contributions do not fit on the grid, the spectra of S1 have cusps in the tails. The tails of the finite difference spectra do not contain cusps but fall off sharply, probably because the finite difference operator in the convective terms, Eq. (1), acts as an implicit

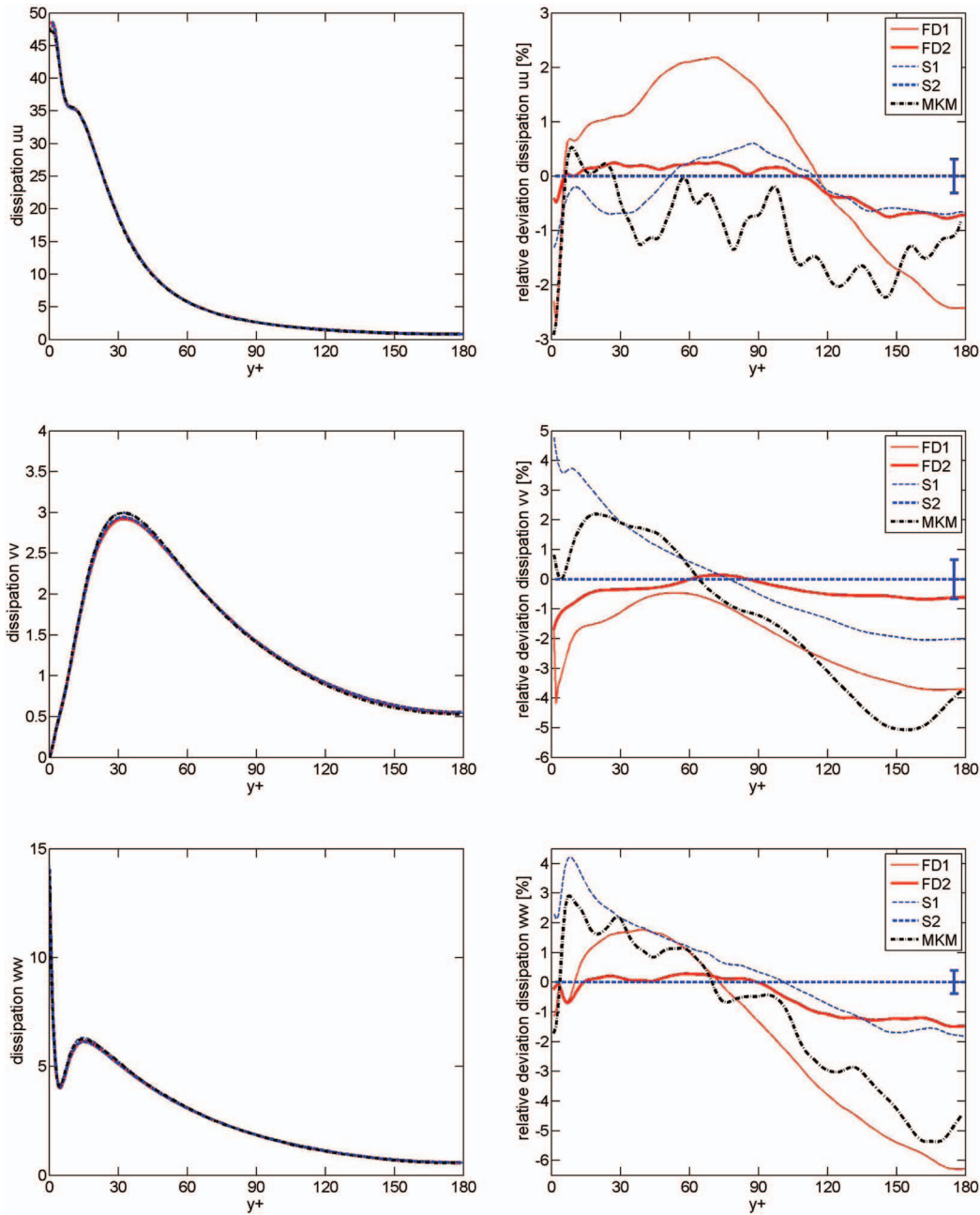


FIG. 4. Components of the dissipation for FD1 (thin solid), FD2 (thick solid), S1 (thin dashed), S2 (thick dashed), and MKM (thick dashed-dotted). Left:  $\epsilon_u$  (top),  $\epsilon_v$  (middle), and  $\epsilon_w$  (bottom). Right: the corresponding relative deviations  $\delta Q[\text{FD1}; S2]$ ,  $\delta Q[\text{FD2}; S2]$ ,  $\delta Q[\text{S1}; S2]$ ,  $\delta Q[\text{S2}; S2]$ , and  $\delta Q[\text{MKM}; S2]$  (%), where  $Q$  is  $\epsilon_u$  (top),  $\epsilon_v$  (middle), or  $\epsilon_w$  (bottom).

filter over the nonlinear transfer to the highest wavenumbers. However, also the spectra of FD1 are too high and have too shallow slope in a region between peak and tail. The fortunate consequence of these overestimations at resolved wavenumbers is that FD1 and S1 do provide reasonable estimates for the integral of the spectrum, which is via Parseval's theorem related to the integral of the square velocity derivative considered. Surprisingly, the premultiplied pressure spectra of S1 and FD1 hardly display overestimated contributions at large wavenumbers (except in the MKM case).

In summary, above figures show that the increased resolution in cases FD2 and S2 leads to better spectra. The curves of the refined cases FD2 and S2 coincide up to large wavenumbers. Overall, the

TABLE II. Maximum relative differences in percent for the 8 quantities shown on line 1. Line 2 is the estimate of the maximum statistical relative error at  $T = 200$ . Lines 3–6 are the absolute maxima of the relative deviation curves shown in Figs. 1–4. Lines 7 and 8 show the absolute maximum of relative differences between the case with constant volume flow (S1a) and two cases with constant forcing.

$Q$	$U$	$u_{rms}$	$v_{rms}$	$w_{rms}$	$p_{rms}$	$\epsilon_u$	$\epsilon_v$	$\epsilon_w$
$\max \delta Q[\text{FD1a}; \text{FD1}] $	0.1	0.4	0.4	0.3	0.4	0.3	0.7	0.4
$\max \delta Q[\text{FD1}; \text{S2}] $	0.8	1.0	1.7	2.0	2.0	2.7	5.2	6.3
$\max \delta Q[\text{FD2}; \text{S2}] $	0.1	0.3	0.6	0.4	0.5	0.8	1.8	1.5
$\max \delta Q[\text{S1}; \text{S2}] $	0.4	0.8	2.5	1.2	1.6	1.3	4.9	4.2
$\max \delta Q[\text{MKM}; \text{S2}] $	0.3	2.7	3.5	2.4	3.1	2.9	5.1	5.4
$\max \delta Q[\text{S1a}; \text{S1}] $	0.2	0.6	1.3	1.1	0.6	1.2	3.2	2.9
$\max \delta Q[\text{S1a}; \text{S2}] $	0.2	0.8	1.3	0.8	1.1	2.4	2.6	2.5

spanwise spectra appear to be less critical than the streamwise spectra, but also the spanwise spectra benefit from the increased resolution. To ensure that also the smallest scales in first-order spatial derivatives are well-resolved it is recommended to use the maximum grid spacings of FD2 or S2 as listed in Table I. Since these numbers are expressed in wall units (normalized with  $\delta_v = H/Re_\tau$ ) they can also be used as a guideline for simulations at higher Reynolds number.

The peak wavenumber of the dissipation spectrum  $k_{peak}$  is by definition the wavenumber at which the slope of the energy spectrum equals  $-2$ . Since at this point the energy spectrum decreases faster than  $k^{-5/3}$ , the peak is in the dissipative range. The non-logarithmic spectra shown in Fig. 7

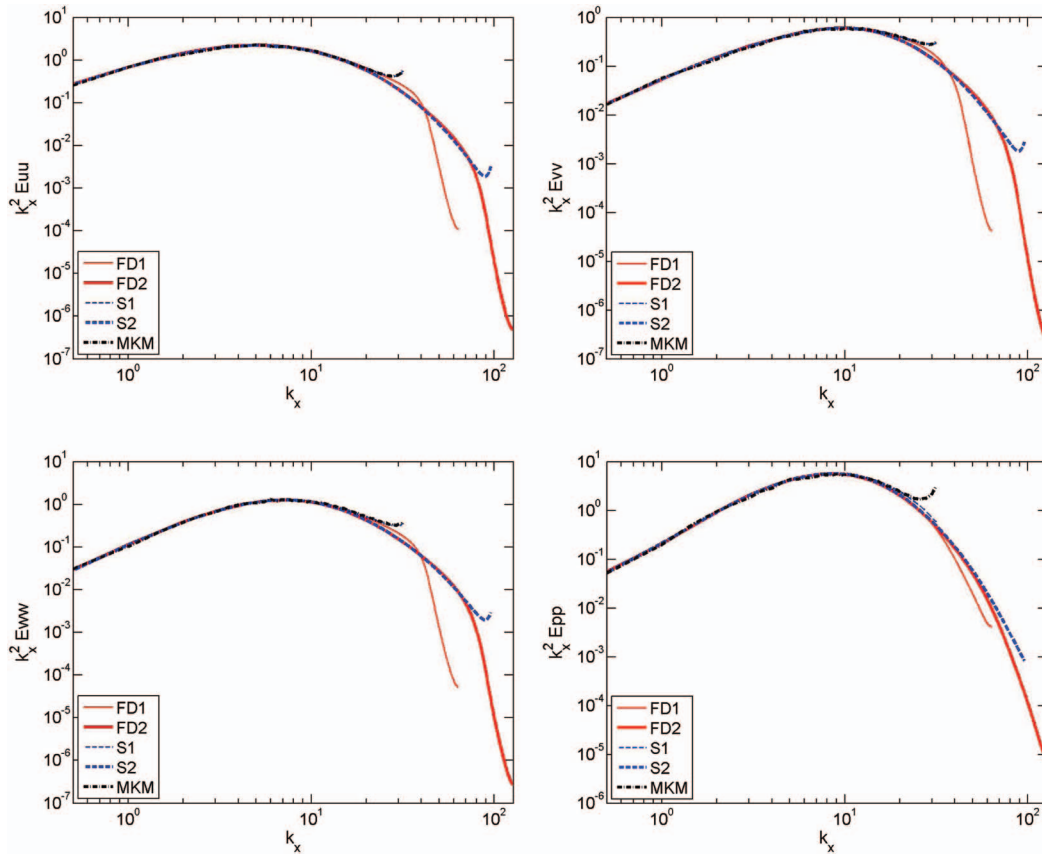


FIG. 5. Pre-multiplied streamwise spectra for  $u$ ,  $v$ ,  $w$ , and  $p$ , at  $y^+ = 30$ . FD1 (thin solid), FD2 (thick solid), S1 (thin dashed), S2 (thick dashed), and MKM (thick dashed-dotted).

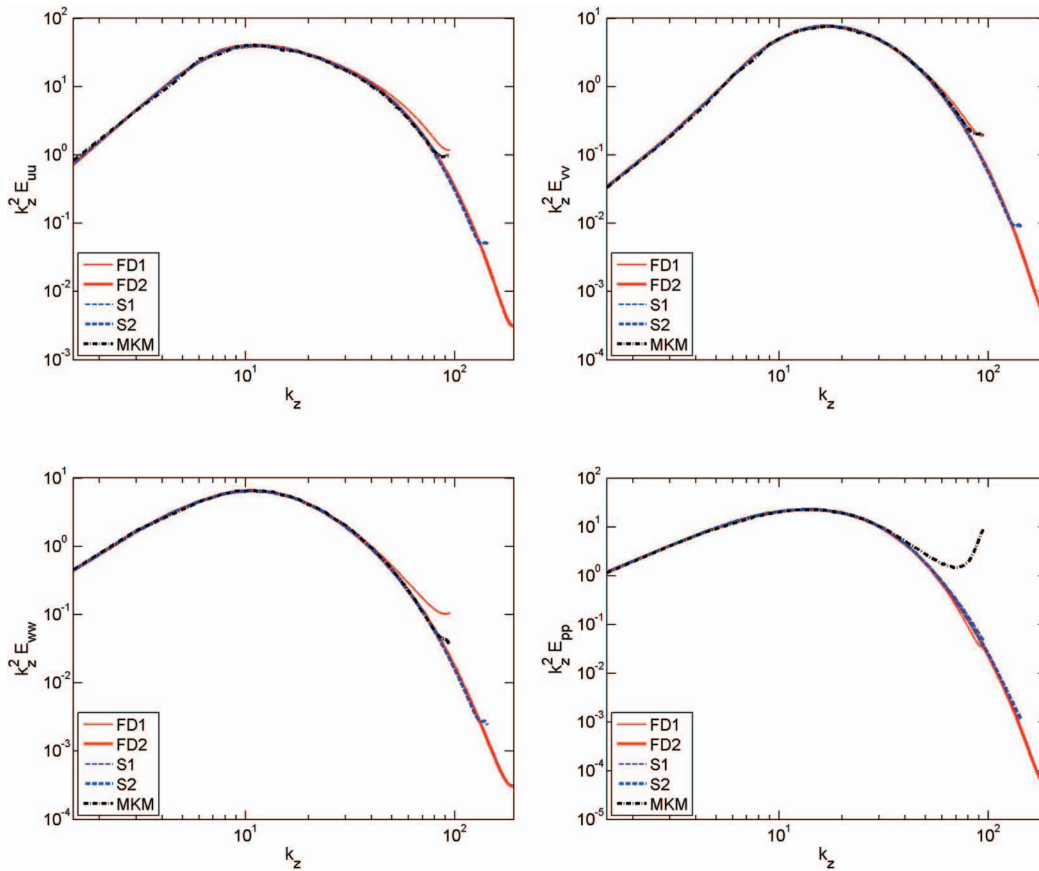


FIG. 6. Premultiplied spanwise spectra for  $u$ ,  $v$ ,  $w$ , and  $p$ , at  $y^+ = 30$ . FD1 (thin solid), FD2 (thick solid), S1 (thin dashed), S2 (thick dashed), and MKM (thick dashed-dotted).

indicate that the wavenumbers  $k > k_{peak}$  contribute considerably more to the dissipation than the wavenumbers  $k < k_{peak}$ , thus  $k_{peak}$  seems to be closer to the beginning of the dissipative range than to the end. It is interesting to compare the length scale that corresponds to  $k_{peak}$  with the Kolmogorov length scale,  $\eta = (\nu^3/\epsilon)^{1/4}$ , which is the characteristic length scale of eddies dominated by viscosity. For this purpose, we define a length scale by  $d = 2\pi/k_{peak}$ , which is the wavelength corresponding to  $k_{peak}$ . More specifically, we define  $d_{u,x} = 2\pi/k_{peak,u,x}$ , which is the wavelength corresponding

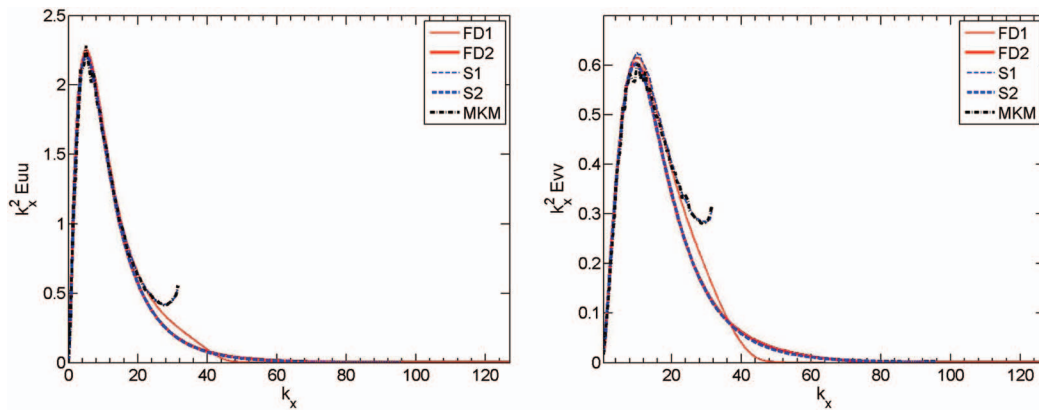


FIG. 7. Premultiplied streamwise spectra for  $u$  and  $v$  at  $y^+ = 30$ , without logarithmic scaling. FD1 (thin solid), FD2 (thick solid), S1 (thin dashed), S2 (thick dashed), and MKM (thick dashed-dotted).

TABLE III. Length scales derived from the peaks of premultiplied spectra, compared with Kolmogorov length scale  $\eta$ , for various values of  $y^+$  and normalized with the wall unit  $\delta_v = H/Re_\tau$ . Also the Taylor microscale  $\lambda$  (based on  $u'$  and  $\partial u'/\partial x$ ) and  $Re_\lambda = u'\lambda/\nu$  are shown.

$y^+$	$d_{u,x}^+$	$d_{v,x}^+$	$d_{w,x}^+$	$d_{p,x}^+$	$d_{u,z}^+$	$d_{v,z}^+$	$d_{w,z}^+$	$d_{p,z}^+$	$d_{min}^+$	$\eta^+$	$d_{min}/\eta$	$\lambda^+$	$Re_\lambda$
10	377	226	151	151	94	94	47	94	47	1.71	28	75.9	192
30	226	151	119	126	94	108	69	84	69	1.91	36	49.3	110
90	226	133	126	133	151	151	108	126	108	2.79	39	44.5	57.8
180	188	141	126	141	151	188	126	151	126	3.69	34	43.3	34.4

to the Fourier wavenumber  $k_{peak, u, x}$ , which is defined as the peak wavenumber of  $k_x^2 E_{uu}$ . In the same way we define a length scale  $d_{u, z}$ , and we do the same for  $v$ ,  $w$ , and  $p$ . These eight length scales, normalized with  $\delta_v = H/Re_\tau$ , are shown in Table III, for various distances from the wall. The minimum of the eight length scales is denoted by  $d_{min}$ . The Kolmogorov length scale, a Taylor microscale, and the Reynolds number based on that Taylor microscale are also included. First we observe that the peak length scales are strongly anisotropic in the near-wall region, while the variation among the eight peak length scales is relatively small in the center of the channel. Second, we observe that, for given  $y^+$ , the minimum peak length scale of the dissipation spectra ( $d_{min}/\eta$ ) is much larger than the Kolmogorov length scale (roughly 30 times larger). This is consistent with high-resolution simulations of homogeneous isotropic turbulence: it can be deduced from Fig. 5 in Ref. 21 that  $k_{peak} \approx 0.2\eta$  if  $k_{peak}$  is defined as the wavenumber at which the slope of the energy spectrum equals  $-2$ , see also Refs. 22 and 23. This corresponds to a wavelength  $2\pi/k_{peak} \approx 10\pi\eta$ . The Kolmogorov length scale seems to be at the far end of the dissipative range of turbulence. It is remarked that the Kolmogorov length scale is based on dimensional analysis; the characteristic length scale of eddies dominated by viscosity could be  $(\nu^3/\epsilon)^{1/4}$  multiplied with a constant larger than 1. Third, we observe that the Taylor microscale  $\lambda$ , which is defined as  $(\overline{u'u'}/(\partial u'/\partial x)^2)^{1/2}$ , is not larger but smaller than most peak length scales (compare, for example,  $d_{u, x}$ ). This behaviour is due to the fact that the Taylor microscale of a single wave  $\sin(kx)$  is equal to  $1/k$ , which is a factor  $2\pi$  smaller than the wavelength  $2\pi/k$ .

## V. DISTINCT TERMS IN THE MOMENTUM EQUATIONS

The momentum equation is given by

$$\partial \mathbf{u} / \partial t = -\mathbf{u} \cdot \nabla \mathbf{u} - \nabla p + \nu \nabla^2 \mathbf{u} + \mathbf{f}. \quad (5)$$

The four terms on the right-hand side are the convective term, the pressure term, the viscous term, and the forcing term. The sum of these four terms is the Eulerian acceleration. The sum of the last three terms is the Lagrangian acceleration  $D\mathbf{u}/Dt = \partial \mathbf{u} / \partial t + \mathbf{u} \cdot \nabla \mathbf{u}$ . Since the forcing term represents a streamwise pressure gradient, we include  $\mathbf{f}$  into  $-\nabla p$ , and we call  $-\nabla p + \mathbf{f}$  also the pressure term. Since  $\mathbf{f}$  is constant in the simulations considered in this section, the inclusion of  $\mathbf{f}$  does not affect the fluctuation of the pressure term. We found some literature on acceleration statistics of turbulent channel flow. Measurements of the acceleration at a single value of  $y$  showed that the Eulerian acceleration becomes much smaller in a reference frame moving with the bulk velocity.<sup>24</sup> In addition, profiles for the Eulerian acceleration, Lagrangian acceleration, and the convective term were extracted from DNS at  $Re_\tau = 360$  and  $Re_\tau = 720$ .<sup>25</sup> The relevance of statistics of Eulerian and Lagrangian accelerations in anisotropic turbulence is discussed in Ref. 26. In the following, we show the acceleration profiles at  $Re_\tau = 180$ , and assess their reproducibility and accuracy. In addition, we include statistics for the separate pressure and viscous terms, and we report the velocity of the reference frame for which the peak fluctuation of the convective terms is minimal.

The profiles of the mean and of the root-mean-square fluctuation of the three components of each term are shown in Fig. 8, for the simulations FD1, FD2, S1, and S2. The root-mean square fluctuation of a quantity  $q$  is defined by  $q_{rms} = \overline{q'^2} = \overline{q^2} - \overline{q}^2$ . In cases FD1 and FD2, the profiles shown are based on the same discretization as in the Navier-Stokes code. In the post-processing of

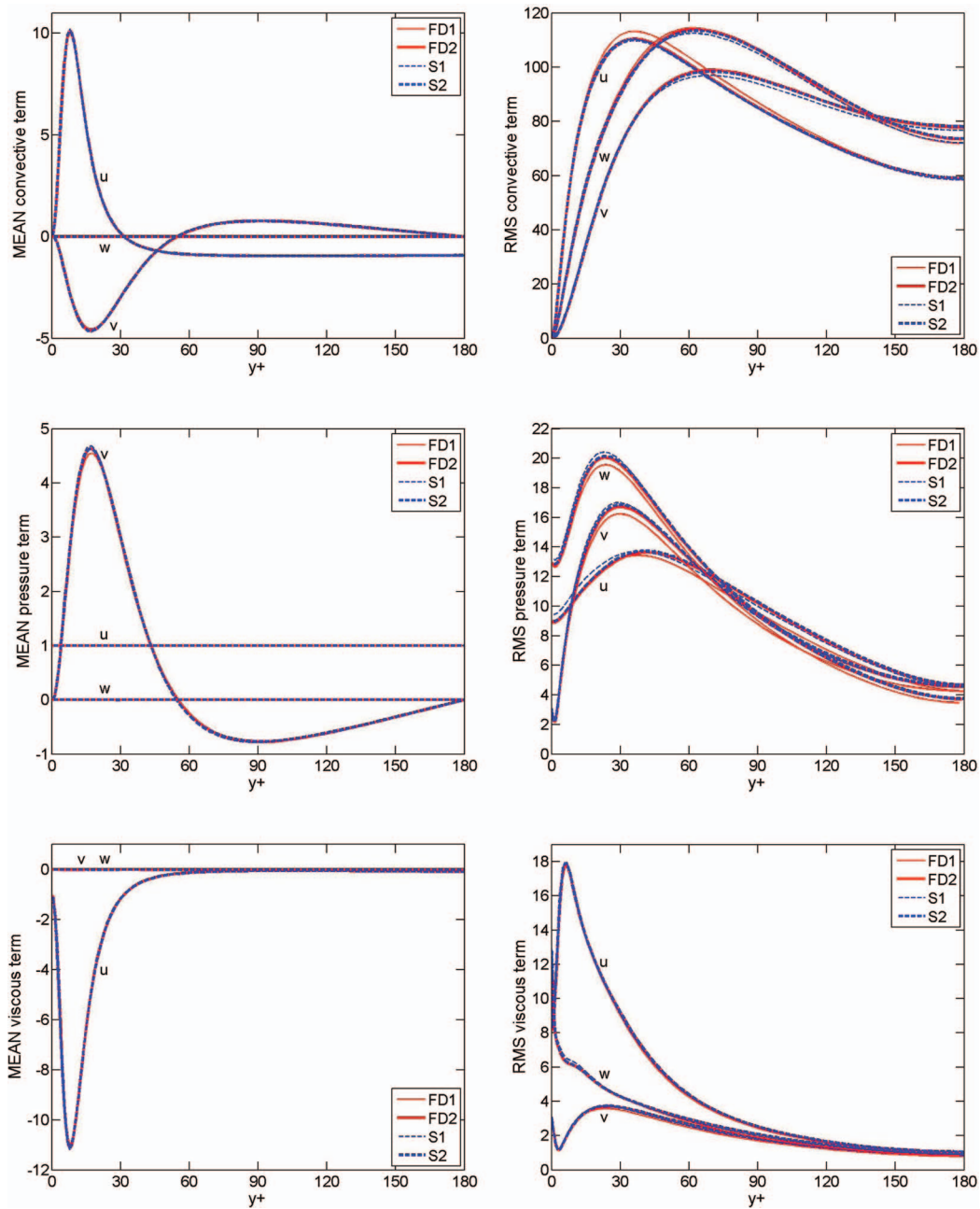


FIG. 8. Means (left) and fluctuations (right) of convective terms (top), pressure terms (middle), and viscous terms (bottom). The symbols  $u$ ,  $v$ , and  $w$  refer to  $u$ -equation,  $v$ -equation, and  $w$ -equation, respectively. FD1 (thin solid), FD2 (thick solid), S1 (thin dashed), and S2 (thick dashed).

S1 and S2, the products  $-\mathbf{u} \cdot \nabla \mathbf{u}$  and the products  $(-\mathbf{u} \cdot \nabla u_i)^2$ ,  $(\partial p / \partial x_i)^2$ ,  $(v \nabla^2 u_i)^2$  and the planar averages are computed in physical space on the  $3/2$ -grid mentioned in Sec. III.

The mean profiles of the nine quantities are shown on the left-hand side of Fig. 8. The mean convective term in the  $u$ -equation represents the normal derivative of the Reynolds shear stress,  $-\partial \overline{u'v'} / \partial y$ , and is balanced by the sum of the mean pressure term and the mean viscous term  $v \nabla^2 \overline{u}$ . The mean convective term in the  $v$ -equation represents the normal derivative  $-\partial \overline{v'v'} / \partial y$ , which is balanced by the mean pressure term  $-\partial \overline{p} / \partial y$ . For each mean quantity, the four simulations produce identical profiles on the scale of the present figures. Compared to the mean quantities, the fluctuations of the nine quantities, shown on the right-hand side of Fig. 8, show much stronger dependence on the

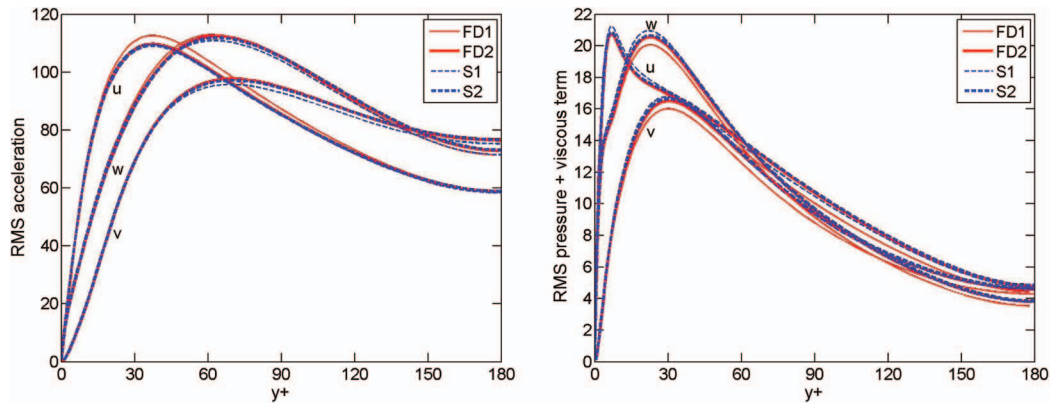


FIG. 9. Left: fluctuations of the Eulerian acceleration,  $d\mathbf{u}/dt$ . Right: fluctuations of the Lagrangian accelerations,  $D\mathbf{u}/Dt$ . The symbols  $u$ ,  $v$ , and  $w$  refer to  $u$ -equation,  $v$ -equation and  $w$ -equation, respectively. FD1 (thin solid), FD2 (thick solid), S1 (thin dashed), and S2 (thick dashed).

numerical method and resolution. However, the fluctuation profiles of the two refined simulations, FD2 and S2, do coincide on the scale of these figures. Thus, the reproducibility of these statistics is also confirmed.

Figure 8 shows that the fluctuation of the convective term is much larger than the fluctuation of the pressure term. The fluctuation of the pressure force is generally larger than the fluctuation of the viscous force. However, for the streamwise component in the near-wall region ( $y^+ < 30$ ), the fluctuation of the pressure force of the streamwise component is smaller than the viscous force. Due to the dominance of the fluctuation of the convective term over the fluctuation of the sum of the pressure and viscous force, the fluctuations of the Eulerian acceleration are much larger than the fluctuations of the Lagrangian acceleration, as shown in Fig. 9. The Eulerian acceleration was obtained as the sum of the convective, pressure, and viscous terms. The mean of the Eulerian acceleration (the sum of the quantities shown on the left-hand side of Fig. 8) should be zero for each component. Numerically, the absolute maximum of the mean Eulerian acceleration was less than 0.01, for each of the four simulations, *i.e.*, less than 0.1% of the maximum value of the mean convective term. Thus, the mean momentum balance is accurately satisfied in each case.

That the fluctuation of Eulerian acceleration is much larger than the fluctuation of the Lagrangian acceleration was also reported in Refs. 24 and 25, as mentioned above. The observation can be expressed as

$$|Du_i/Dt| \ll |\partial u_i/\partial t|. \quad (6)$$

This is related to Taylor's hypothesis of frozen turbulence.<sup>27</sup> Taylor's hypothesis states that  $\partial u_i/\partial t + \mathbf{U} \cdot \nabla u_i = 0$ , *i.e.*,  $|\partial u_i/\partial t + \mathbf{U} \cdot \nabla u_i| \ll |\partial u_i/\partial t|$ , which is assumed to be valid if the convection velocity  $\mathbf{U}$  is much larger than the velocity fluctuations. The hypothesis provides a relation between  $\partial \mathbf{u}/\partial x$  and  $\partial \mathbf{u}/\partial t$  and has been frequently used in experiments. The convection velocity  $\mathbf{U}$  is usually the local mean flow, while in (6) the convection velocity is the local instantaneous velocity.

It is well known that the solution of the Navier-Stokes equations are Galilean invariant. However, the convective term and the Eulerian acceleration are not Galilean invariant terms, although the sum  $\partial \mathbf{u}/\partial t + \mathbf{u} \cdot \nabla \mathbf{u}$  is Galilean invariant. Thus, the ratio of left-hand and right-hand sides of inequality (6) changes after a Galilean transformation. Galilean invariance means that if the Navier-Stokes problem is formulated for velocity  $\hat{\mathbf{u}}$  and translated spatial coordinates  $\hat{\mathbf{x}} = \mathbf{x} + \mathbf{c}t$ , and if no-slip boundary condition  $\hat{\mathbf{u}} = -\mathbf{c}$  and initial condition  $\hat{\mathbf{u}}_0 = \mathbf{u}_0 - \mathbf{c}$  are imposed, then the original solution  $\mathbf{u}$  is equal to  $\hat{\mathbf{u}} + \mathbf{c}$ , provided the translative velocity  $\mathbf{c}$  is constant. In case  $\mathbf{c} = (c, 0, 0)$  and  $c$  is constant, the Galilean transformed convective term is equal to

$$-\hat{\mathbf{u}} \cdot \hat{\nabla} \hat{\mathbf{u}} = -\mathbf{u} \cdot \nabla \mathbf{u} + c \partial \mathbf{u}/\partial x. \quad (7)$$

The difference between the transformed and the original convective term is just a linear term,  $c \partial \mathbf{u}/\partial x$ . Similarly, the Galilean transformed Eulerian acceleration becomes  $\partial \mathbf{u}/\partial t + c \partial \mathbf{u}/\partial x$ .

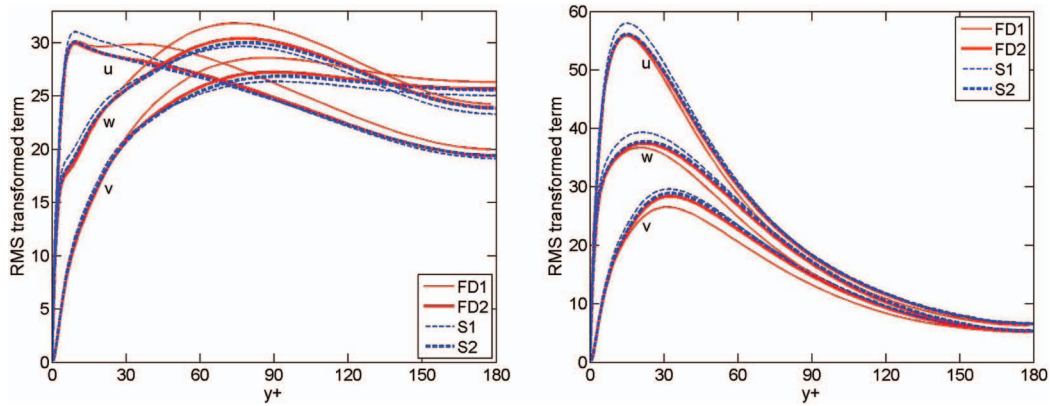


FIG. 10. Fluctuations of the three components of the Galilean-transformed convective term,  $(\mathbf{u} - \mathbf{c}) \cdot \nabla \mathbf{u}$ . Left:  $\mathbf{c} = (12.20u_\tau, 0, 0)$ . Right:  $\mathbf{c} = (18.28u_\tau, 0, 0)$ . The symbols  $u$ ,  $v$ , and  $w$  refer to  $u$ -equation,  $v$ -equation, and  $w$ -equation, respectively. FD1 (thin solid), FD2 (thick solid), S1 (thin dashed), and S2 (thick dashed).

Figure 10 shows the fluctuations of the convective term after two Galilean transformations,  $c = 12.20u_\tau$  and  $c = 18.28u_\tau$ . For the first value of  $c$ , which is lower than the bulk velocity ( $15.70u_\tau$ ), the maximum of the three peak fluctuations of the convective term is minimal. The second value is equal to the mean velocity at the centerline. In the first case the peak value of the fluctuation of the convective term reduces with a factor 4 compared to the original fluctuation of the convective term in Fig. 8. In the second case the peak is reduced with about a factor 2, but centerline values show much larger relative reduction and become of the same order of magnitude as the centerline values of the fluctuations of the pressure and viscous terms. It appears that a dominant part of the fluctuation of the convective term (and of the Eulerian acceleration) in the original case can be represented by a linear term  $-c\partial\mathbf{u}/\partial x$ .

Kim and Hussain<sup>28</sup> computed the streamwise propagation velocity of velocity fluctuations and other quantities in turbulent channel flow at  $Re_\tau = 180$ . They defined the streamwise propagation velocity of a quantity  $q$  by  $\Delta x/\Delta t$ , where  $\Delta x$  was such that the correlation between  $q(x + \Delta x, y, z, t + \Delta t)$  and  $q(x, y, z, t)$  was maximum for given  $\Delta t$ . They found that the propagation velocity of the velocity fluctuation was equal to the mean velocity for  $y^+ > 15$ , while for  $y^+ < 15$  the propagation velocity was approximately 55% of the centerline velocity ( $\approx 10u_\tau$ ). Del Álamo and Jiménez<sup>29</sup> revisited Taylor's hypothesis and computed a velocity profile  $C(y)$ , such that for each  $y$  that ratio of the root mean square of  $\partial u/\partial t + C(y)\partial u/\partial x$  and the root mean square of  $\partial u/\partial t$  was minimal. This  $C(y)$  can be interpreted as the representative convection velocity profile for which Taylor's approximation gives the lowest error. For  $Re_\tau = 550$  they found that  $C(y)$  was somewhat lower than the mean velocity in the bulk region, but higher than the mean velocity in the near wall region. The present constant frame velocity  $c = 12.20u_\tau$  for which the peak fluctuation of the convective term lies in between the minimum and maximum of the propagation velocity profile of Ref. 28, and also in between the minimum and maximum of the  $C(y)$ -profile of Ref. 29.

After Galilean transformation with the centerline velocity ( $c = U_c = 18.28u_\tau$ ), the fluctuation of the transformed convective term at the center (Fig. 10(right)) is approximately the same as the fluctuation of  $D\mathbf{u}/Dt$  at the center (Fig. 9(right)). They are not exactly the same, since the fluctuation of  $\partial\hat{\mathbf{u}}/\partial t$ , the transformed Eulerian acceleration, is not zero. Let us consider the turbulence at the centerline of the Galilean transformed case of Fig. 9(right) in some more detail. The mean velocity of the transformed case is zero at the centerline. The fluctuation of the Lagrangian acceleration is not modified by the transformation, thus the centerline values of  $D\hat{\mathbf{u}}/Dt$  are those shown in Fig. 9(right): 4.8, 4.6, and 3.8, for  $\hat{u}$ -,  $\hat{v}$ -, and  $\hat{w}$ -components, respectively. The centerline values of the fluctuation of the transformed convective term in Fig. 9(right) are 6.6, 5.3, and 5.3. The fluctuation of  $\partial\hat{\mathbf{u}}/\partial t$  is not shown in the figures, but the centerline values have been computed: 5.1, 4.9, and 4.8, for  $\hat{u}$ -,  $\hat{v}$ -, and  $\hat{w}$ -components, respectively. These values are of the same order as the centerline values of the Lagrangian acceleration. In this context, it is interesting to mention Tennekes' theory on the applicability of Taylor's hypothesis to small eddies advected by the sweeping motion of large

eddies in flows with zero mean velocity.<sup>30</sup> The mean velocity is zero at the centerline of the Galilean transformed case of Fig. 9(right). The ratio of Eulerian time microscale  $T_{E,\hat{u}}$  and Lagrangian time microscale  $T_{L,\hat{u}}$  of  $\hat{u}$  is defined as<sup>30</sup>

$$T_{E,\hat{u}}/T_{L,\hat{u}} = \frac{\overline{(\partial\hat{u}/\partial t)^2}^{1/2}}{\overline{(D\hat{u}/Dt)^2}^{1/2}}. \quad (8)$$

Analogous time scale ratios can be defined for  $\hat{v}$  and  $\hat{w}$ . Tennekes<sup>30</sup> expected  $T_E/T_L \ll 1$  (compare Eq. (6)) and derived

$$T_E/T_L \approx \frac{\frac{4}{3}(\epsilon\nu)^{1/4}}{u'u' + v'v' + \hat{w}'w'}. \quad (9)$$

By substitution of the numbers mentioned in the previous paragraph into definition Eq. (8) we find that  $T_E/T_L$  equals 0.94, 0.94, and 0.79, respectively, numbers that are not much smaller than 1. However, the evaluation of Eq. (9) leads to a much lower value,  $T_E/T_L \approx 0.24$ . The computation based on the definition of  $T_E/T_L$  indicates that the advection of small by large eddies is not important at the centerline where  $Re_\lambda = 34$  (Table III). The numbers of the two expressions for  $T_E/T_L$  are consistent with results from simulations of homogeneous isotropic turbulence. For  $Re_\lambda = 38$ , Table 6 in Ref. 31 implies  $T_E/T_L = 1/0.92 = 1.09$  for definition (8), and  $T_E/T_L = 1/4.07 = 0.25$  for approximation (9). For  $Re_\lambda = 243$ , Table 2 in Ref. 32 implies  $T_E/T_L = (3.54/17.05)^{1/2} = 0.46$  for definition (8). Thus the trend in Tennekes' theory is correct;  $T_E/T_L$  reduces if the Reynolds number is increased.

## VI. HIGHER-ORDER STATISTICS

The non-Gaussianity of turbulence can be quantified by the value of third- and higher-order moments of variables. The so-called skewness and flatness are derived from the third- and fourth-order moments. For a given quantity  $q$ , the skewness is  $S(q) = \overline{q^3}/(\overline{q^2})^{3/2}$ , and the flatness is  $F(q) = \overline{q^4}/(\overline{q^2})^2$ . If the probability distribution of  $q$  is Gaussian, then  $S(q) = 0$  and  $F(q) = 3$ . In this section we investigate non-Gaussianity of channel flow turbulence by considering the skewness and flatness of several quantities.

The skewness that received most attention in turbulence research is probably the skewness of the longitudinal velocity derivative  $\partial u/\partial x$ . In homogeneous turbulence this quantity is typically between  $-0.5$  and  $-0.6$ ,<sup>33,36</sup> while values between  $-0.3$  and  $-0.4$  have been measured in a turbulent boundary layer.<sup>34</sup> A negative skewness means that large negative values appear more frequently than large positive values. Negative skewness of  $\partial u/\partial x$  has been related to vortex stretching and the energy cascade from large to small scales.<sup>35</sup> No DNS-data for the velocity derivative skewness in inhomogeneous turbulence was found in the literature.

The equation for  $\partial u/\partial x$ , derived from the Navier-Stokes equations, can be written in the form

$$\frac{D}{Dt} \frac{\partial u}{\partial x} = -\left(\frac{\partial u}{\partial x}\right)^2 + R, \quad (10)$$

with

$$R = -\frac{\partial v}{\partial x} \frac{\partial u}{\partial y} - \frac{\partial w}{\partial x} \frac{\partial u}{\partial z} - \frac{\partial^2 p}{\partial x^2} + \nu \nabla^2 \frac{\partial u}{\partial x}. \quad (11)$$

Since the first term on the right-hand side of (10) is always negative, negative  $\partial u/\partial x$  tends to become more negative and positive  $\partial u/\partial x$  less positive, along fluid pathlines. Of course the complicated term  $R$  cannot be neglected, but it is likely that the negative sign of the first term has some influence on the statistical properties of  $\partial u/\partial x$ . The mean of  $\partial u/\partial x$  cannot be influenced (it is zero by definition of the channel flow), but the probability distribution of  $\partial u/\partial x$  becomes negatively skewed.

The equation for  $(\partial u/\partial x)^2$  can be derived from (10):

$$\frac{\partial}{\partial t} \left(\frac{\partial u}{\partial x}\right)^2 + \nabla \cdot \left(\mathbf{u} \left(\frac{\partial u}{\partial x}\right)^2\right) = -2\left(\frac{\partial u}{\partial x}\right)^3 + 2R \frac{\partial u}{\partial x}. \quad (12)$$

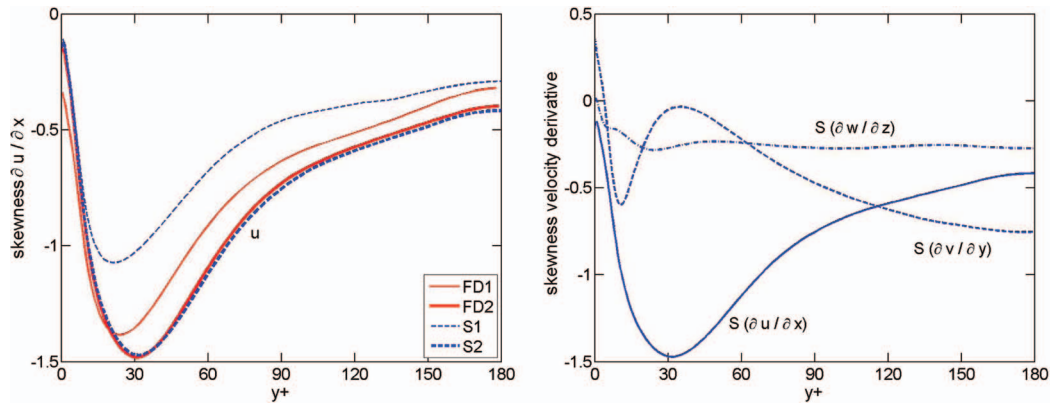


FIG. 11. Skewness of the diagonal components of the velocity gradient tensor. Left:  $S(\partial u / \partial x)$  from databases FD1, FD2, S1, and S2. Right:  $S(\partial u / \partial x)$ ,  $S(\partial v / \partial y)$ , and  $S(\partial w / \partial z)$  from database S2.

One of the nine contributions to the turbulent dissipation is  $\epsilon_{ux} = \overline{v(\partial u' / \partial x)^2}$ . Since  $\partial u / \partial x = \partial u' / \partial x$  in the present channel flow configuration, the equation for  $\epsilon_{ux}$  directly follows from (12):

$$\frac{\partial}{\partial t} \epsilon_{ux} + \nabla \cdot (\mathbf{u} \epsilon_{ux}) = -2 S_{ux} \frac{\epsilon_{ux}^{3/2}}{\nu^{1/2}} + 2\nu R \frac{\partial u}{\partial x}, \quad (13)$$

where  $S_{ux}$  denotes the skewness of  $\partial u / \partial x$ . The last equation provides another reason why  $S_{ux}$  is interesting; negative  $S_{ux}$  represents production of turbulent dissipation. The same applies to the skewnesses of  $\partial v / \partial y$  and  $\partial w / \partial z$ .

Profiles of the skewness of the diagonal components of the velocity gradient tensor are shown in Fig. 11. Fig. 11(left) shows that sufficient resolution is important to compute these quantities accurately. That FD2 and S2 coincide, while FD1 and S1 are very different, is an indication that the resolution of these two cases is sufficient to show these quantities. In the remainder of this section only profiles of case S2 are shown. It is striking that  $S(\partial u / \partial x)$  attains a value of  $-1.5$  around  $y^+ = 30$ , much more negative than the skewness in homogeneous turbulence. At the same location the skewness of the normal diagonal component is approximately zero (Fig. 11(right)). This may be related to the strong anisotropy of the turbulence in the near-wall region, where the fluctuation of  $u'$  is relatively large and important near-wall structures such as streaks and streamwise vortices are very elongated in the streamwise direction.

Figure 12 shows the contour plot of a snapshot of  $u'$  at  $y^+ = 30$ . We observe structures of high-speed and low-speed fluid, elongated in the  $x$ -direction. The second plot in Fig. 12 zooms into a region of the first plot. Around  $x^+ = 1550$ , we observe a high-speed structure which has collided into a low-speed structure, and as a result the front-side of the high-speed structure shows an inward deformation. At that point  $(\partial u / \partial x)^3$  displays a negative peak. If a structure with  $u' > 0$  and structure with  $u' < 0$  are on the same line in the  $x$ -direction, and if they approach each other, then the fast structure is by definition behind the slow structure, and  $\partial u / \partial x$  is by definition negative. The fluid in between the structures is squeezed and pushed aside, into the  $y$ - or  $z$ -direction or into both directions. In Fig. 12(bottom) the fluid is primarily pushed into the  $y$ -direction, which means that  $\partial v / \partial y$  is positive and larger than  $\partial w / \partial z$ . This type of behaviour is consistent with the observation that at  $y^+ = 30$  the skewness of  $\partial v / \partial y$  is hardly negative. The pressure fluctuation tends to be positive at the front side of the structure where  $-(\partial u / \partial x)^3$  peaks. This implies that the pressure strain  $p'(\partial u / \partial x)$  is negative at this point and redistributes kinetic energy to at least one of the other two velocity components.

Figure 13 shows the skewness and flatness of the primary fluctuations,  $u'$ ,  $v'$ ,  $w'$ , and  $p'$ . These have also been reported in Ref. 1, but there are quantitative differences in the flatnesses. The flatness of the normal velocity,  $F(v')$ , converges to 29.2 on the wall, compared to 22 reported in Ref. 1. Furthermore,  $F(p')$  peaks at 8.8 in the center region, compared to approximately 7 in

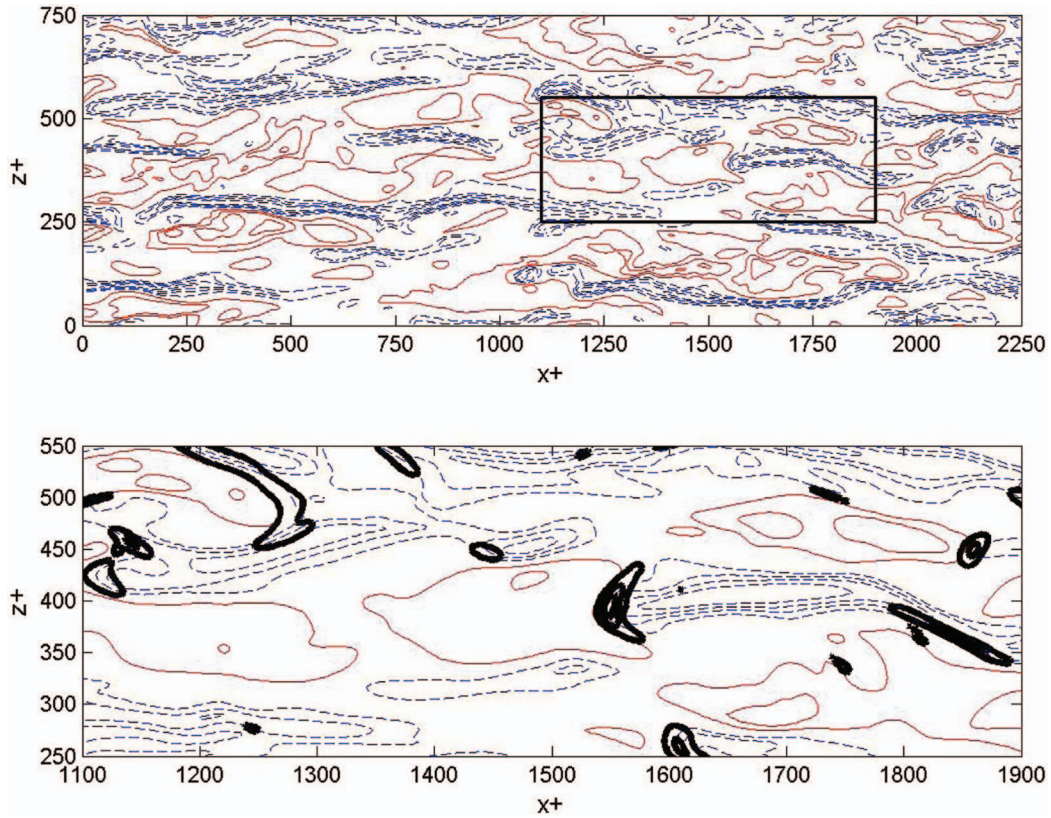


FIG. 12. Top: Contours of a snapshot of  $u'$  in the plane  $y^+ = 30$ , normalized with the maximum  $|u'|$  in the plane, from database FD2. The dashed (blue) contour levels are  $-0.2$ ,  $-0.4$ ,  $-0.6$ , and  $-0.8$ ; the solid (red) contour levels are  $0.2$ ,  $0.4$ ,  $0.6$ , and  $0.8$ . Bottom: An enlargement of the rectangle in the top figure. The thick (black) contours are the contours of  $(\partial u'/\partial x)^3$  with negative values and depict the regions that lead to negative skewness of  $\partial u'/\partial x$ .

Fig. 18 in Ref. 1. The negative skewness of  $u'$  at  $y^+ = 30$  is consistent with the contours of the streaky structures in Fig. 12 (regions with  $u'$  display stronger peaks than regions with positive  $u'$ ).

The flatness measures the intermittency of a quantity. A strongly intermittent signal at some point is dormant most of the time; there are periods with activity, but most of the time the activity is small. It is remarkable that the maximum intermittency of the velocity occurs near the wall, while the maximum intermittency of the pressure occurs in the bulk region. The maximum flatness of the

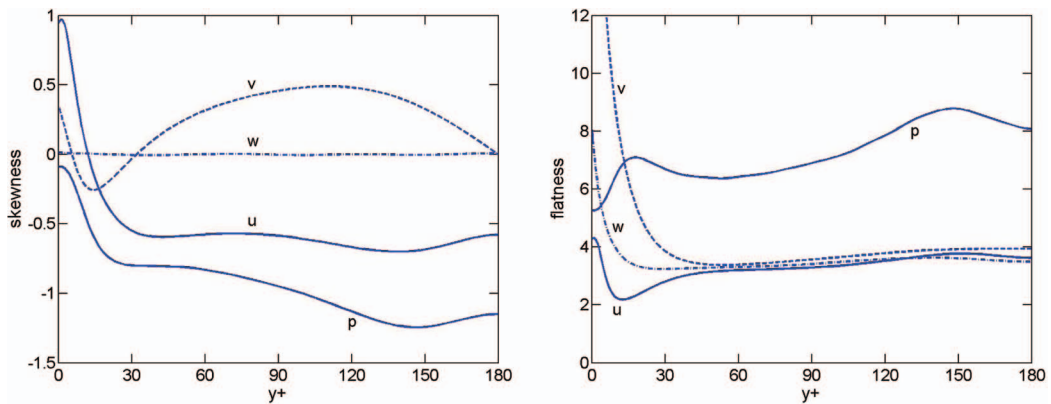


FIG. 13. Skewness (left) and flatness (right) of the primary fluctuations  $u'$ ,  $v'$ ,  $w'$ , and  $p'$ , from database S2.  $F(v')$  converges to 29.2 as  $y^+ \rightarrow 0$ .

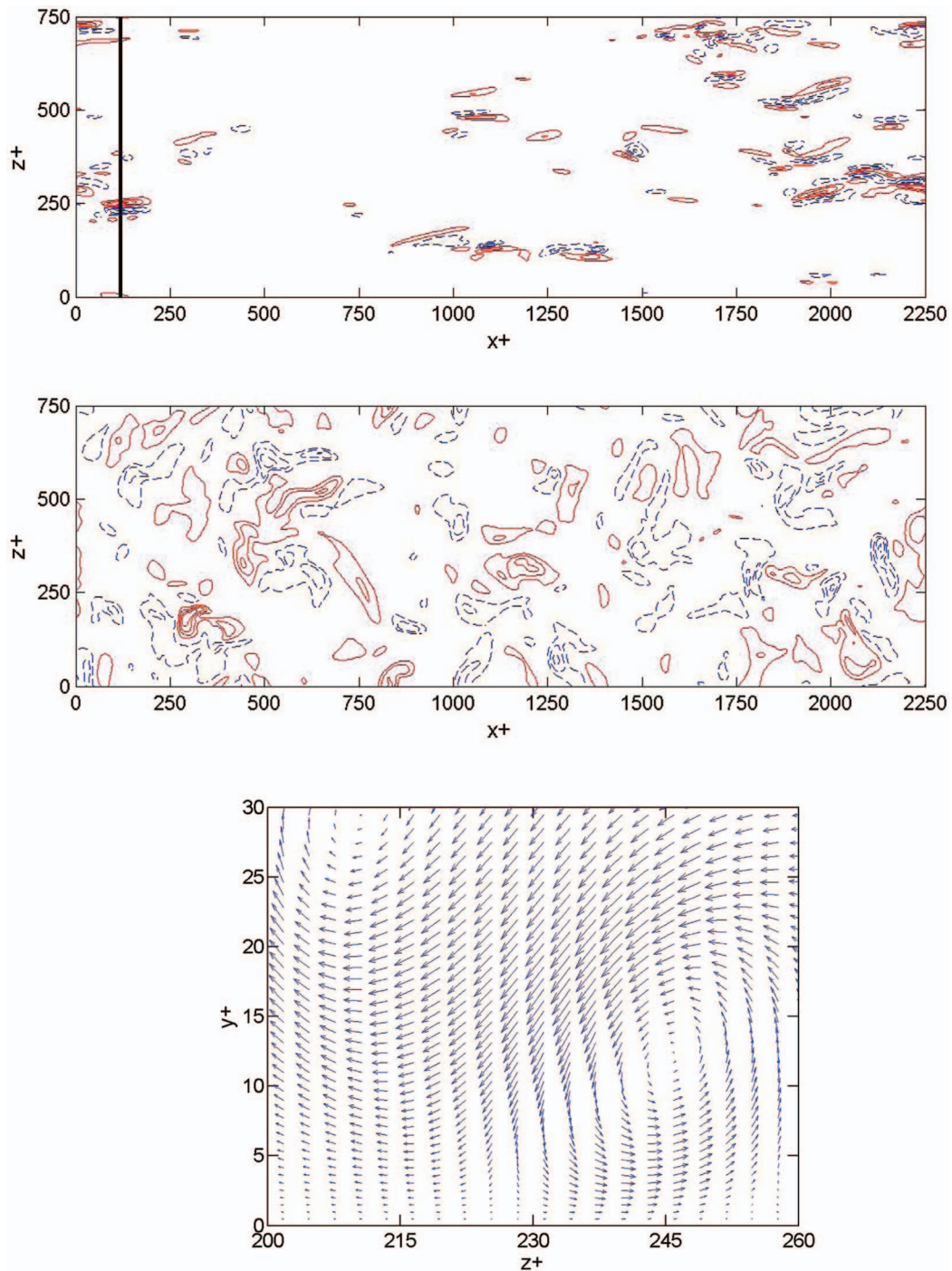


FIG. 14. Contours of a snapshot of  $v'$  in the plane  $y^+ = 3$  (top) and the plane  $y^+ = 180$  (middle), normalized with the maximum  $|v'|$  in each plane, from database FD2. The dashed (blue) contour levels are  $-0.2$ ,  $-0.4$ ,  $-0.6$ , and  $-0.8$ ; the solid (red) contour levels are  $0.2$ ,  $0.4$ ,  $0.6$ , and  $0.8$ . The solid vertical line at  $x^+ = 120$  in the top figure denotes the perpendicular plane shown in the velocity vector plot (bottom).

pressure, 8.8, appears to be higher than in isotropic turbulence. According to Refs. 37–39 the flatness of the pressure in isotropic turbulence varies between 4.7 (low Reynolds number) and 7.1 (higher Reynolds number).

The most striking observation from the flatness profiles is that  $v'$  is very intermittent near the wall. The behaviour of the flatness profile of  $v'$  is illustrated by snapshots of  $v'$  in planes parallel to the wall (Fig. 14): regions with noticeable normal velocity fluctuation are scarce in the viscous sublayer ( $y^+ = 3$ ), compared to the center of the channel ( $y^+ = 180$ ). The normal velocity is strongly intermittent at  $y^+ = 3$  ( $F(v') \approx 17$ ), while it is weakly intermittent at  $y^+ = 180$  ( $F(v') = 3.9$ ). Structures with relatively large normal velocity fluctuation can hardly penetrate into the viscous sublayer, but occasionally a vortex is pushed down toward the wall. These are typically streamwise vortices, see, for example, the vortex centered at  $z^+ \approx 245$  in the vector plot in Fig. 14. The edge of the vortex causes negative and positive normal velocity fluctuations in the viscous sublayer, which last as long as the viscous force permits.

## VII. CONCLUSIONS

DNS databases were compared to assess the accuracy and reproducibility of standard and non-standard turbulence statistics of incompressible plane channel flow at  $Re_\tau = 180$ . The domain size was the same as in Moser, Kim, and Mansour.<sup>2</sup> Two fundamentally different codes, a staggered finite difference code (FD) and a spectral code (S), were used. Standard resolution was used in simulations FD1 and S1, enhanced resolution was used in simulations FD2 and S2. The statistical averaging time was long, typically  $200H/u_\tau$ . The maximum relative deviation between the mean flow profiles of FD2 and S2 was about 0.1%. The maximum relative deviation between root-mean-square values of velocity and pressure fluctuations of FD2 and S2 was about 0.6%. The maximum relative deviation of the three components of the turbulent dissipation was about 1.8%. An analysis of dissipation spectra demonstrated that the enhanced resolution is necessary for an accurate representation of the smallest physical scales in the turbulent dissipation. The enhanced resolution corresponds to the following grid-spacings in terms of channel half-width  $H$  and  $Re_\tau$ : streamwise  $6H/Re_\tau$ , spanwise  $4H/Re_\tau$ , and in the normal direction  $3H/Re_\tau$  at the center, and about  $H/Re_\tau$  at  $y^+ = 12$ . These are the numbers for the spectral method. For the finite difference method these grid-spacings should be multiplied with  $3/4$ .

There are several conclusions with respect to the physics of turbulent channel flow. First, the observed reproducibility supports the hitherto unproven theoretical hypothesis that the statistically stationary state of incompressible turbulent channel flow is unique. Second, the length scale based on the peaks of the dissipation spectra appeared to be much larger than the Kolmogorov length scale, roughly 30 times. Third, the computed means and fluctuations of the convective, pressure, and viscous terms in the momentum equation showed that the fluctuation of the convective term was much larger than the fluctuation of the pressure force and that at most locations the fluctuation of the pressure force was larger than the fluctuation of the viscous force. Fourth, the Galilean transformation that leads to minimum peak fluctuation of the convective term was determined. The peak fluctuation of the convective terms is minimum in a reference frame moving with streamwise velocity  $12.20u_\tau$ . Fifth, Taylor's hypothesis and the ratio of Eulerian and Lagrangian turbulence time scales were discussed. Sixth, an analysis of higher-order statistics showed that the skewness of the longitudinal derivative of the streamwise velocity is stronger than expected ( $-1.5$  at  $y^+ = 30$ ). The derivative skewness was related to coherent structures. Seventh, the intermittency of fluctuations of primary variables was discussed. The strong near-wall intermittency of the normal velocity was related to streamwise vortices penetrating into the viscous sublayer.

<sup>1</sup>J. Kim, P. Moin, and R. Moser, "Turbulence statistics in fully developed channel flow at low Reynolds number," *J. Fluid Mech.* **177**, 133–166 (1987).

<sup>2</sup>R. D. Moser, J. Kim, and N. N. Mansour, "Direct numerical simulations of turbulent channel flow up to  $Re_\tau = 590$ ," *Phys. Fluids* **11**, 943–945 (1999).

<sup>3</sup>N. D. Sandham, "Resolution requirements for direct numerical simulation of near-wall turbulent flow using finite differences," Technical Report QMW-EP-1097, Queen Mary and Westfield College, University of London, 1994.

<sup>4</sup>H. Abe, H. Kawamura, and Y. Matsuo, "Direct numerical simulation of a fully developed turbulent channel flow with respect to Reynolds number dependence," *ASME J. Fluids Eng.* **123**, 382–393 (2001).

- <sup>5</sup>J. C. del Álamo and J. Jiménez, "Spectra of the very large anisotropic scales in turbulent channels," *Phys. Fluids* **15**, L41–L43 (2003).
- <sup>6</sup>Z. W. Hu, C. L. Morfey, and N. D. Sandham, "Wall pressure and shear stress spectra from direct numerical simulations of channel flow up to  $Re\tau = 1440$ ," *AIAA J.* **44**, 1541–1549 (2006).
- <sup>7</sup>J. Meyers and P. Sagaut, "Is plane-channel flow a friendly case for the testing of large-eddy simulation subgrid-scale models?," *Phys. Fluids* **19**, 048105 (2007).
- <sup>8</sup>S. Hoyas and J. Jiménez, "Reynolds number effects on the Reynolds-stress budgets in turbulent channels," *Phys. Fluids* **20**, 101511 (2008).
- <sup>9</sup>M. Kozuka, Y. Seki, and H. Kawamura, "Direct numerical simulation of turbulent heat transfer with a high spatial resolution," *Int. J. Heat Fluid Flow* **30**, 514–524 (2009).
- <sup>10</sup>J. Kim, "Progress in pipe and channel flow turbulence, 1961–2011," *J. Turbulence* **13**, N45, 1–19 (2012).
- <sup>11</sup>N. Gilbert and L. Kleiser, "Near-wall phenomena in transition to turbulence," in *Near-Wall Turbulence: 1988 Zoran Zaric Memorial Conference* (Hemisphere, New York, 1990), pp. 7–27.
- <sup>12</sup>N. D. Sandham and L. Kleiser, "The late stages of transition to turbulence in channel flow," *J. Fluid Mech.* **245**, 319–348 (1992).
- <sup>13</sup>F. E. Harlow and J. E. Welsh, "Numerical calculation of time-dependent viscous incompressible flow of fluid with free surface," *Phys. Fluids* **8**, 2182 (1965).
- <sup>14</sup>Y. Morinishi, T. S. Lund, O. V. Vasilyev, and P. Moin, "Fully conservative higher order finite difference schemes for incompressible flow," *J. Comput. Phys.* **143**, 90–124 (1998).
- <sup>15</sup>R. W. C. P. Verstappen and A. E. P. Veldman, "Symmetry-preserving discretization of turbulent flow," *J. Comput. Phys.* **187**, 343–368 (2003).
- <sup>16</sup>A. Jameson and T. J. Baker, "Solution of the Euler equations for complex configurations," AIAA Paper No. 83-1929, 1983.
- <sup>17</sup>K. Horiuti and T. Itami, "Truncation error analysis of the rotational form for the convective terms in the Navier-Stokes equation," *J. Comput. Phys.* **145**, 671–692 (1998).
- <sup>18</sup>J. G. M. Kuerten, C. W. M. van der Geld, and B. J. Geurts, "Turbulence modification and heat transfer enhancement by inertial particles in turbulent channel flow," *Phys. Fluids* **23**, 123301 (2011).
- <sup>19</sup>B. J. Geurts and J. G. M. Kuerten, "Ideal stochastic forcing for the motion of particles in large-eddy simulation extracted from direct numerical simulation of turbulent channel flow," *Phys. Fluids* **24**, 081702 (2012).
- <sup>20</sup>P. R. Spalart, R. D. Moser, and M. M. Rogers, "Spectral methods for the Navier-Stokes equations with one infinite and two periodic directions," *J. Comput. Phys.* **96**, 297–324 (1991).
- <sup>21</sup>Y. Kaneda, T. Ishihara, M. Yokokawa, K. Itakura, and A. Uno, "Energy dissipation rate and energy spectrum in high resolution direct numerical simulations of turbulence in a periodic box," *Phys. Fluids* **15**, L21–L24 (2003).
- <sup>22</sup>Z. S. She, S. Chen, G. Doolen, R. H. Kraichnan, and S. A. Orszag, "Reynolds number dependence of isotropic Navier-Stokes turbulence," *Phys. Rev. Lett.* **70**, 3251–3254 (1993).
- <sup>23</sup>P. K. Yeung and Y. Zhou, "Universality of the Kolmogorov constant in numerical simulations of turbulence," *Phys. Rev. E* **56**, 1746–1752 (1997).
- <sup>24</sup>K. T. Christensen and R. J. Adrian, "The velocity and acceleration signatures of turbulent channel flow," *J. Turbulence* **3**, N23 (2002).
- <sup>25</sup>L. Chen, S. W. Coleman, J. C. Vassilicos, and Z. Hu, "Acceleration in turbulent channel flow," *J. Turbulence* **11**, N41 (2010).
- <sup>26</sup>J. J. H. Brouwers, "Eulerian short-time statistics of turbulent flow at large Reynolds number," *Phys. Fluids* **16**, 2300–2308 (2004).
- <sup>27</sup>G. I. Taylor, "The spectrum of turbulence," *Proc. R. Soc. London, Ser. A* **164**, 476–490 (1938).
- <sup>28</sup>J. Kim and F. Hussain, "Propagation velocity of perturbations in turbulent channel flow," *Phys. Fluids A* **5**, 695–705 (1993).
- <sup>29</sup>J. C. del Álamo and J. Jiménez, "Estimation of turbulent convection velocities and corrections to Taylor's approximation," *J. Fluid Mech.* **640**, 5–26 (2009).
- <sup>30</sup>H. Tennekes, "Eulerian and Lagrangian time microscales in isotropic turbulence," *J. Fluid Mech.* **67**, 561–567 (1975).
- <sup>31</sup>P. K. Yeung and S. B. Pope, "Lagrangian statistics from direct numerical simulations of isotropic turbulence," *J. Fluid Mech.* **207**, 531–586 (1989).
- <sup>32</sup>A. Tsinober, P. Vedula, and P. K. Yeung, "Random Taylor hypothesis and the behavior of local and convective accelerations in isotropic turbulence," *Phys. Fluids* **13**, 1974–1984 (2001).
- <sup>33</sup>S. Tavoularis, J. C. Bennett, and S. Corrsin, "Velocity-derivative skewness in small Reynolds number, nearly isotropic turbulence," *J. Fluid Mech.* **88**, 63–69 (1978).
- <sup>34</sup>H. Ueda and J. O. Hinze, "Fine-structure turbulence in the wall region of a turbulent boundary layer," *J. Fluid Mech.* **67**, 125–143 (1975).
- <sup>35</sup>U. Frisch, *Turbulence: The Legacy of A. N. Kolmogorov* (Cambridge University Press, Cambridge, 1995).
- <sup>36</sup>T. Ishihara, Y. Kaneda, M. Yokokawa, K. Itakura, and A. Uno, "Small-scale statistics in high-resolution direct numerical simulation of turbulence: Reynolds number dependence of one-point velocity gradient statistics," *J. Fluid Mech.* **592**, 335–366 (2007).
- <sup>37</sup>A. Pumir, "A numerical study of pressure fluctuations in three-dimensional, incompressible, homogeneous, isotropic turbulence," *Phys. Fluids* **6**, 2071–2083 (1994).
- <sup>38</sup>P. Vedula and P. K. Yeung, "Similarity scaling of acceleration and pressure statistics in numerical simulations of isotropic turbulence," *Phys. Fluids* **11**, 1208–1220 (1999).
- <sup>39</sup>N. Cao, S. Chen, and G. D. Doolen, "Statistics and structures of pressure in isotropic turbulence," *Phys. Fluids* **11**, 2235–2250 (1999).